International Journal of Concrete Structures and Materials
DOI 10.1186/s40069-018-0250-y
ISSN 1976-0485 / eISSN 2234-1315

Multiphysics Modeling and Simulation of Strength Development and Distribution in Cemented Tailings Backfill Structures

Liang Cui[1)] and Mamadou Fall[2),*]

(Received June 24, 2017, Accepted January 19, 2018)

Abstract: Cemented paste backfill structures are complex underground cementitious structures. After fresh cemented paste backfill (CPB; a mix of tailings, binder and water) is poured into underground stopes (mined-out voids), its strength which is a key mechanical design criterion of CPB structures, gradually develops with time. The development of CPB strength is governed by the coupled thermo-hydro-mechanical-chemical (THMC) processes in the CPB mass. Therefore, to assess and predict the changes to CPB strength and its distribution within the CPB mass, a multiphysics model on CPB strength is proposed in this study, and has been successfully validated against a series of experimental data. Then, the validated model is used to investigate the changes in the strength of CPB structure under various influential factors in the field (e.g., backfilling strategy, inclination angle of stope, and filling rate). The obtained results provide better insight into the process of the strength increase and spatial distribution in CPB structures as well as contribute to more cost-effective engineering designs of CPB structures.

Keywords: cemented paste backfill, concrete, mine, THMC, multiphysics, strength, tailings.

1. Introduction

Due to its significant environmental (Aldhafeeri and Fall 2016), technical (Suazo et al. 2016a) and economic (Cui and Fall 2015a) benefits, cemented paste backfill (CPB; a cementitious material made of unclassified tailings (fine man-made aggregates), hydraulic binders, and water) has been widely applied in underground mines (Suazo et al. 2016b). Since the failure of CPB structures can have substantial financial ramifications and cause severe injuries and/or fatalities (Nasir and Fall 2009), mechanical stability has been considered as a significant design criterion of CPB structures. To satisfy the design criterion of mechanical stability of CPB structures in underground mines, CPB strength is typically in the range of 0.5–2.5 MPa (Jefferis and Wilson 2012). However, increases in CPB strength is substantially affected by the coupled thermo-hydro-mechanical-chemical (THMC) processes that occur in the CPB mass as shown in Fig. 1 and briefly discussed below.

Specifically, as binder hydration progresses, the resultant bonds between the tailings particles directly contribute to the development of CPB strength (Fall et al. 2010; Yılmaz et al. 2014). Moreover, due to the temperature dependence of binder hydration (Barnett et al. 2006; Cui and Fall 2016b), the thermal process can affect the development of CPB strength as well. For the hydraulic process, the pore-water consumption caused by binder hydration (Cui and Fall 2017b) and water drainage through the barricade (a retaining structure built at the floor base) (Cui and Fall 2017a) can cause the build-up of suction and thus increase the effective stress which can further improve the CPB strength. In addition, stope (underground mine excavation or cavity) backfilling can be carried out in many ways and thus affects the consolidation behavior of CPB (Cui and Fall 2016c). As a result, the void ratio related properties, such as hydraulic conductivity, will change as well. Correspondingly, the pore-water pressure (PWP) and thus effective stress will be affected with the development of consolidation. In addition, as indicated in Fig. 1, there are weak couplings (i.e., the dash line in Fig. 1) amongst the physical processes in CPB mass. The weak coupling or weakly coupled processes refers to the fact that the effect of a process on another is not significant. For instance, with the development of consolidation (i.e., the mechanical process), the hydraulic conductivity and fluid flow behavior (i.e., the hydraulic process) will be significantly affected. However, the effect of consolidation on the chemical processes is not significant, i.e. the effect is weak. Similarly, the binder hydration (chemical process) has a significant effect on the hydraulic process (e.g., change in pore water pressure due to the water consumption by cement hydration), whereas the hydraulic processes only weakly affect the binder hydration. Therefore, to accurately assess the development of CPB strength, the coupled THMC processes must be fully considered.

As the mechanical stability of CPB structures is important, there have been extensive studies that examine CPB strength at both the laboratory and in situ scales. These studies have

[1)]Department of Civil Engineering, Lakehead University, Thunder Bay, ON P7B 5E1, Canada.
[2)]Department of Civil Engineering, University of Ottawa, Ottawa, ON K1N 6N5, Canada.
*Corresponding Author; E-mail: mfall@uottawa.ca
Copyright © The Author(s) 2018

Published online: 19 March 2018

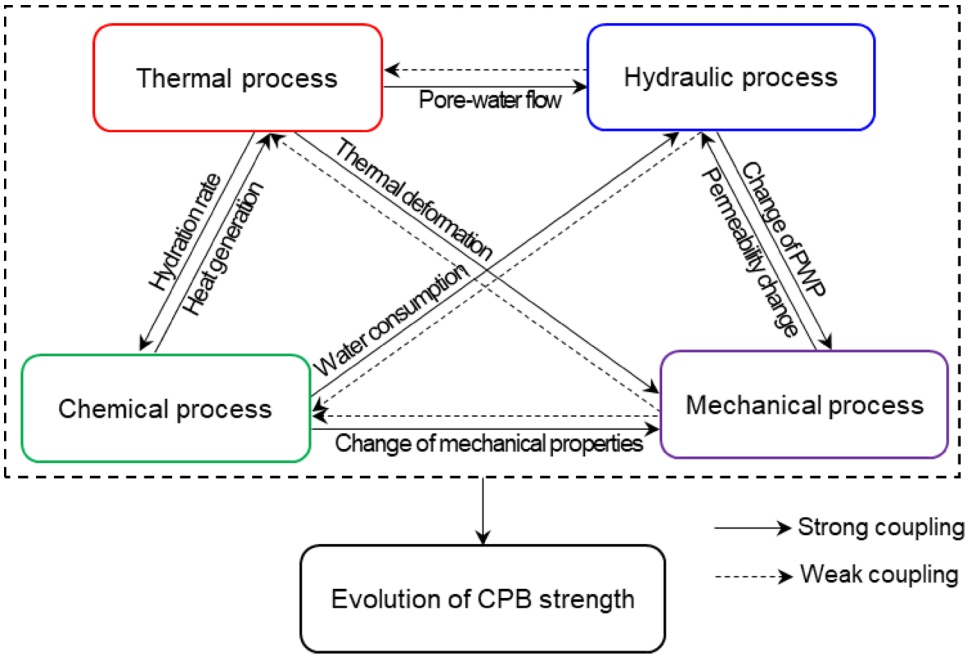

Fig. 1 Schematic diagram of primary controlling mechanisms of changes to CPB strength.

identified several factors that significantly affect the development of CPB strength, such as the curing temperature (e.g., Fall et al. 2010; Wang and Fall 2014), mixture recipe (e.g., Ercikdi et al. 2009; Hamberg et al. 2015), sulphate content in the tailings (e.g., Fall et al. 2008; Li and Fall 2016), curing pressure (e.g., Ghirian and Fall 2015; Yilmaz et al. 2011), drainage conditions (e.g., Belem et al. 2006; Cui and Fall 2016b), and filling strategy (e.g., Ghirian and Fall 2016b). These experimental findings have provided in-depth insight into the changes to CPB strength. Moreover, several empirical and partially coupled mathematical models have been developed to predict the changes in CPB strength based on the controlling mechanisms. For instance, Xu et al. (2017b) proposed a logarithmic relationship between the CPB strength and electrical resistivity based on the laboratory measurements. Through ultrasonic pulse velocity tests, several empirical relationships (e.g., Xu et al. 2017a; Yılmaz and Ercikdi 2016) between CPB strength and ultrasonic pulse velocity have been established. In addition, to predict the CPB strength, Qi et al. (2018) proposed an original technique via a combination of the artificial neural network and particle swarm optimization. Apart from the empirical mathematical models, several partially coupled Multiphysics models have been developed to assess the strength developed in CPB. For instance, Nasir and Fall (2010) developed a hybrid numerical/analytical model to predict the changes in CPB strength with variations in the temperature and progression of binder hydration. This model can evaluate the changes in temperature in CPB and binder hydration with curing time. However, the proposed model on the strength of CPB did not take into consideration all of the main coupled THMC processes that occur in CPB structures which affect their strength development. Mozaffaridana (2011) proposed a maturity method to incorporate the combined effects of curing time and temperature into the prediction of CPB strength. However, this model requires measurements of CPB temperature during the prediction periods and does not consider the effects of the mixture recipe and mechanical load (e.g., stress) and deformation (e.g., consolidation); that is, the model is empirical. Similarly, based on a regression analysis on the unconfined compressive strength (UCS) values for different curing ages, an empirical correlation between CPB strength, curing time and sample size was proposed by Yilmaz et al. (2015). Therefore, to accurately assess and predict the strength of CPB material subjected to complex multiphysics loadings, a fully coupled THMC model on CPB strength development is required. This THMC model on the strength of CPB will contribute to an optimal design of CPB structures and reliable analysis of their mechanical stability. Therefore, the aims of this paper include:

(1) To develop a multiphysics model on the strength of CPB, which fully considers the effects of coupled THMC processes, and
(2) To investigate the changes in CPB strength in the field under different curing and loading conditions.

2. Modelling Approach

To develop the multiphysics model on CPB strength, the prerequisite is to quantitatively simulate: (1) the mechanical behavior (especially the stress–strain relationship obtained from UCS testing) and (2) changes in the mechanical properties. For the CPB materials, it has been found that chemical hardening and strain hardening/softening become more apparent with curing time (Belem et al. 2000; Fall et al. 2007). Therefore, an evolutive elastoplastic model is needed to understand the stress–strain relationship of CPB with

curing time. Correspondingly, if the hardening/softening behavior can be accurately evaluated (i.e., the mathematical description of the expansion (hardening) and contraction (softening) of the yield surface in stress space with the development of plastic strain), the CPB strength (i.e., the peak point of stress–strain curve) can be determined by using the first derivative test on the hardening/softening parameter with respect to the cumulative plastic strain. Moreover, to describe the effects of coupled THMC processes on the changes to the CPB strength, the related mechanical properties (e.g., cohesion and internal friction angle) cannot be considered constant with time (i.e., a predictive function for each mechanical property is required). In addition, it should be noted that CPB strength should be defined in terms of effective stress. Therefore, in the present study, Biot's effective stress is integrated into the derivation of the multiphysics model on CPB strength. Consequently, the pore fluid pressure (hydraulic process), volume change (mechanical process) induced by the consolidation process in CPB, binder hydration (chemical process) process and its temperature dependence (thermal process) are fully considered.

3. Mathematical Formulation

A yield function is required to derive CPB strength. Due to the influence of the binder hydration, the mechanical properties (e.g., cohesion and internal frictional angle) will change with time. Therefore, an evolutive elastoplastic mechanical model based on a modified Drucker–Prager (D–P) yield criterion was proposed by Cui and Fall (2016a). This proposed model is adopted here to derive the model on CPB strength.

$$F = \sqrt{J_2} + \alpha(\xi, \kappa)[I_1 - C(\xi)] = 0 \tag{1}$$

With

$$\alpha(\xi, \kappa) = \frac{2\sin\phi_B(\xi)}{\sqrt{3}[3 + \sin\phi_B(\xi)]} + B_1\{[1 - \exp(-B_2\kappa)] + [B_3\kappa\exp(-B_4\kappa)]\}C(\xi) = 3c_B(\xi)\cdot\cot\phi_B(\xi) \tag{2}$$

where I_1 and J_2 respectively represent the first stress invariant and the second deviatoric stress invariant; α and C denote the material properties of the yield function, and change with degree of binder hydration ξ and cumulative plastic strain κ ($\kappa = \int\sqrt{2/3}d\varepsilon_P d\varepsilon_P$ with plastic strain ε_P), namely $\alpha = \alpha(\xi, \kappa)$ and $C = C(\xi)$; B_i is a material parameter and changes with the degree of binder hydration (i = 1–4); c_B and ϕ_B are the cohesion and internal friction angle of the CPB, which are functions of the degree of binder hydration ($c_B = c_B(\xi)$ and $\phi_B = \phi_B(\xi)$).

It should be noted that CPB strength must be defined in terms of the effective stress, $\boldsymbol{\sigma}'$. Therefore, Biot's effective stress is incorporated into the derivation of the model on CPB strength in the present study:

$$\sigma' = \boldsymbol{\sigma} + (1 - K_b/K_s)\cdot(SP_w + (1 - S)P_a)\boldsymbol{\delta}_{ij} \tag{3}$$

where $\boldsymbol{\sigma}'$ and $\boldsymbol{\sigma}$ denote the Biot's effective stress and total stress tensor, respectively; K_b and K_s respectively represent the bulk modulus of the CPB skeleton and solid phase; S is the degree of saturation; P_w and P_a refer to the pore-water and pore-air pressures; and $\boldsymbol{\delta}_{ij}$ is the Kronecker's delta. It should be noted that the compressive stress is taken to be negative in this study.

For the stress state of CPB under UCS testing, the "true" strength of the CPB, $\boldsymbol{\sigma}_s$, should be defined in terms of the peak value of the axial total stress, $\boldsymbol{\sigma}_{p\_axial}$, pore-water pressure P_w, and pore-air pressure P_a:

$$\boldsymbol{\sigma}_s = \boldsymbol{\sigma}_{p\_axial} + (1 - K_b/K_s)\cdot(SP_w + (1 - S)P_a)\boldsymbol{\delta}_{ij} \tag{4}$$

It should be noted that for the measurement method of the UCS (i.e., uniaxial compressive strength test), the measured peak stress refers to the axial stress applied by using a UCS device, namely, the measured peak stress value equals $\boldsymbol{\sigma}_{p\_axial}$. Correspondingly, the stress invariants can be rewritten in terms of $\boldsymbol{\sigma}_{p\_axial}$:

$$I_1 = \boldsymbol{\sigma}_{p\_axial} \tag{5}$$

$$J_2 = \boldsymbol{\sigma}_{p\_axial}^2 \Big/ 3 \tag{6}$$

Therefore, the peak value of the axial total stress $\boldsymbol{\sigma}_{p\_axial}$ can be solved by substituting Eqs. (5) and (6) into the yield function (i.e., Eq. (1)):

$$\boldsymbol{\sigma}_{p\_axial} = \sqrt{3}C(\xi) \Big/ \left[\sqrt{3} - \frac{1}{\alpha(\xi, \kappa_s)}\right] \tag{7}$$

where κ_s refers to the value of the cumulative plastic strain when $\alpha(\xi, \kappa)$ reaches its peak point. From Eq. (7), it can be observed that for a given degree of hydration, the axial total stress reaches its maximum value when the peak value of $\alpha(\xi, \kappa)$ is obtained. Based on the definition of strain hardening and softening, there is only one inflection point of $\alpha(\xi, \kappa)$ (i.e., the inflection point corresponds to $\alpha(\xi, \kappa_s)$). Then, κ_s can be derived through the first derivative test of $\alpha(\xi, \kappa)$ with respect to the cumulative plastic strain κ, namely:

$$\frac{\partial\alpha(\xi, \kappa)}{\partial\kappa} = 0 \Rightarrow B_2\exp(-B_2\kappa_s) + B_3(1 - B_4\kappa_s)\exp(-B_4\kappa_s) = 0 \tag{8}$$

Then, the value of the cumulative plastic strain when $\alpha(\xi, \kappa)$ reaches its peak point can be derived (details on the derivation of κ_s are provided in Appendix A):

$$\kappa_s = \frac{B_2^2 + B_4 + \sqrt{B_4^2 + B_2^2 B_4 - B_2^4}}{B_2^3} \tag{9}$$

Substituting Eq. (2) into Eq. (7), the peak value of the axial total stress can be written as:

$$\sigma_{p\_axial} = \frac{3\sqrt{3}c_B(\xi)\cdot\cot\phi_B(\xi)}{\sqrt{3}+1\Big/\left\{\frac{2\sin\phi_B(\xi)}{\sqrt{3}[3+\sin\phi_B(\xi)]}+B_1\{[1-\exp(-B_2\kappa_s)]+B_3\kappa_s\exp(-B_4\kappa_s)\}\right\}} \tag{10}$$

Then, the true model on CPB strength can be derived by substituting Eq. (10) into Eq. (4):

$$\sigma_s = \frac{3\sqrt{3}c_B(\xi)\cdot\cot\phi_B(\xi)}{\sqrt{3}+1\Big/\left\{\frac{2\sin\phi_B(\xi)}{\sqrt{3}[3+\sin\phi_B(\xi)]}+B_1\{[1-\exp(-B_2\kappa_s)]+B_3\kappa_s\exp(-B_4\kappa_s)\}\right\}} + (1-K_b/K_s)[SP_w+(1-S)P_a]\delta_{ij} \tag{11}$$

With

$$\kappa_s = \frac{B_2^2+B_4+\sqrt{B_4^2+B_2^2B_4-B_2^2}}{B_2^3}$$

It should be noted that (1) Eq. (11) represents the "true" CPB strength which incorporates the effect of pore pressure into the characterization of CPB strength. However, the common testing method of CPB strength (i.e., the UCS tests) records the axial total stress applied by the UCS device and then directly uses the peak value (i.e., σ_{p_axial}) of the axial total stress to represent CPB strength (i.e., the nominal CPB strength). Therefore, both the nominal (Eq. (10)) and true (Eq. (11)) models on CPB strength are derived in this study, (2) because the tensile stress is considered to be positive in this study, the derived nominal and true CPB strength values from Eqs. (10) and (11) are negative. To follow the convention of strength analysis, a positive value of strength is adopted in the following sections, (3) as demonstrated in Eq. (11), the prediction of CPB strength requires pore pressure values and the corresponding degree of saturation values. Therefore, modelling and simulation of hydraulic processes in CPB are necessary. As previously discussed in the Introduction, CPB behavior is controlled by coupled THMC processes, namely, each physical process interacts with other processes. Hence, defining the hydraulic processes in CPB requires a fully coupled THMC model specific for CPB materials. In this regard, Cui and Fall (2015a) developed a fully coupled THMC model which can be used to predict the pore pressure and degree of saturation. More details on the coupled THMC model can be found in (Cui and Fall 2015a).

4. Determination of Model Parameters

As demonstrated in the model on CPB strength (i.e., Eq. (11)), there are a series of model parameters that need to be determined. As discussed earlier in the Introduction, binder hydration plays a crucial role in the changes of the material properties of CPB. Therefore, a quantitative assessment of the progress of binder hydration should be first carried out. In this study, the exponential model proposed by Schindler and Folliard (2003) is adopted to characterize the development of binder hydration in CPB materials, which fully considers the effect of the mixture recipe (including water-to-cement ratio, addition of fly ash and blast furnace slag, cement type), curing temperature and curing time.

$$\xi(w/c,X_{FA},X_{slag},T,t) = \left(\frac{1.031\cdot w/c}{0.194+w/c}+0.5\cdot X_{FA}+0.30\cdot X_{slag}\right)\times\exp\left\{-\left\{\tau\Big/\int_0^t\exp\left[\frac{E_a}{R}\left(\frac{1}{T_r}-\frac{1}{T}\right)\right]dt\right\}^{\beta}\right\} \tag{12}$$

With

$$\tau = 66.78x_{C_3A}^{-0.154}\cdot x_{C_3S}^{-0.401}\cdot x_{SO_3}\cdot S_{Blaine}^{-0.804}\cdot\exp\left(2.178X_{slag}+9.5X_{FA}X_{FA-CaO}\right)$$

$$\beta = 181.4x_{C_3A}^{0.146}\cdot x_{C_3S}^{0.227}\cdot x_{SO_3}^{0.558}\cdot S_{Blaine}^{-0.535}\cdot\exp\left(-0.647X_{slag}\right)$$

$$E_a(T) = \begin{cases} 33,500+1,470\times(293.15-T) & T<293.15K \\ 33,500 & T\geq 293.15K \end{cases}$$

where $w/wc{\cdot}c$ refers to the water-to-cement ratio; X_{FA} and X_{slag} denote the weight fraction of the fly ash and blast furnace slag to the total binder weight, respectively; T and T_r represent the CPB temperature and its reference temperature; τ and β respectively are the time and hydration shape parameters; E_a is the apparent activation energy; R denotes an ideal gas constant; t is the curing time; x_i represents the mass ratio of the i component to the total binder weight ($i = C_3A$, C_3S and SO_3); and $X_{FA\text{-}CaO}$ is the weight ratio of CaO to fly ash.

As demonstrated in Eq. (11), the CPB cohesion changes with the degree of binder hydration (i.e., $c_B = c_B(\xi)$). To assess the changes in the cohesion of CPB materials, the following predictive function is proposed:

$$c_B(\xi) = \exp(M_{s1}S_T)\cdot(1-S_W)^{M_{s2}\exp(M_{s3}\xi)}\cdot M_{c1}\cdot C_m\cdot\xi^{M_{c2}} \tag{13}$$

where M_{s1}, M_{s2}, M_{s3}, M_{c1} and M_{c2} are fitting parameters; S_T represents the sulfide mass content with respect to the total mass of dry tailings; S_w refers to the sulphate content in the mixing water; and C_m is the cement content with respect to the total solid mass. Based on a regression analysis of the experimental values taken from direct shear tests (DSTs) reported in (Donovan 1999; Ghirian and Fall 2014; Koupouli et al. 2016), $M_{s1} = -9.6$, $M_{s2} = 724.3$, $M_{s3} = -4.553$, $M_{c1} = 9507$ kPa and $M_{c2} = 3.2$ in this study. As shown in Fig. 2, the predicted cohesion is in good agreement with the experimental value ($R^2 = 0.92$) reported by Cui and Fall (2016a) and Sargeant (2008). Moreover, as demonstrated in Eq. (13), the effect of the mixture recipe (cement content), sulphate content in the tailings and mixing water, and binder hydration are incorporated to determine CPB cohesion. In addition, due to the temperature dependence of binder hydration (see Eq. (12)), the effect of the

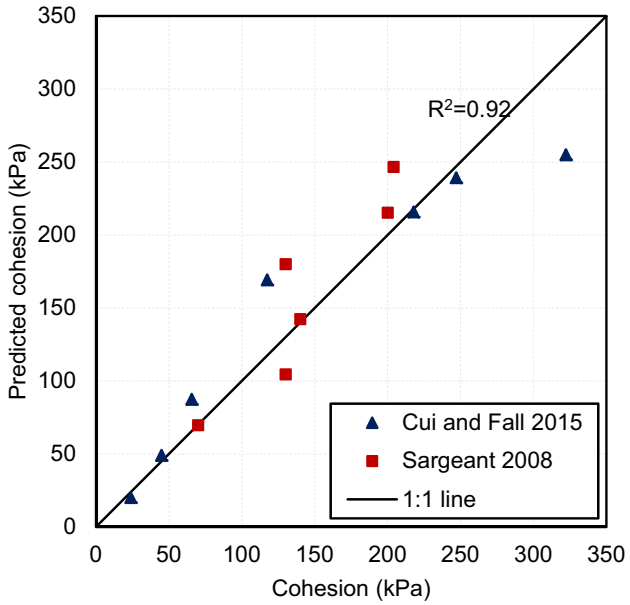

Fig. 2 Experimental versus predicted values of cohesion.

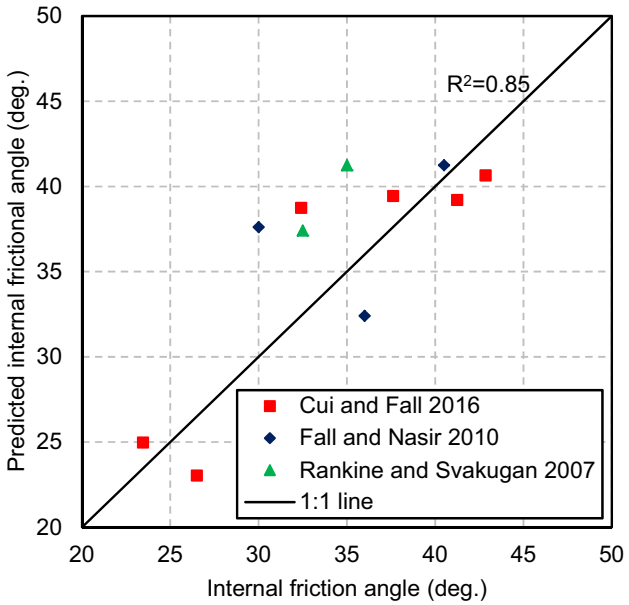

Fig. 3 Experimental versus predicted values of internal friction angle.

thermal process is taken into account for determining CPB cohesion.

Similar to the changes in cohesion, it has been found that the internal friction angle can change with curing time (i.e., progression of binder hydration) (Veenstra 2013). To evaluate the variations of the internal friction angle, the following predictive function is proposed:

$$\phi_B(\xi) = [\exp(N_0 S_T)] \cdot \left(N_1 \xi^{N_2} + N_3 \xi\right) \tag{14}$$

where N_i is a fitting constant ($i = 0$–3) which can be determined through regression analysis on the experimental values of DSTs on CPB samples with different curing times. Based on the reported data of the DSTs (Koupouli et al. 2016; Veenstra 2013), $N_0 = -0.33$, $N_1 = -176.9°$, $N_2 = 2$ and $N_3 = 174.2°$ are adopted in this study. A comparison between the experimental and predicted values of the internal friction angle is presented in Fig. 3. It can be seen that there is a fairly good agreement between the predicted results and measured data published in (Cui and Fall 2016a; Fall and Nasir 2010; Rankine and Sivakugan 2007) ($R^2 = 0.85$).

To evaluate the contribution of the PWP to the changes in CPB strength, the bulk moduli K_b and K_s in Eq. (11) are required. The bulk modulus of the solid phase K_s depends on the type of tailings. The bulk modulus of the porous media K_b can be directly measured through isotropic compression testing (Luo et al. 2015) or determined by using the elastic modulus E and Poisson's ratio υ of CPB (i.e., $K_b = E/E[3(1-\upsilon)].[3(1-\upsilon)]$). In this study, the latter is adopted to describe the changes in K_b. Previous studies on the stress–strain relation in CPB (Fall et al. 2007; Ghirian and Fall 2014; Rankine and Sivakugan 2007) found that the sulphate and cement contents, void ratio and degree of binder hydration have significant impacts on elastic modulus changes. Hence, the following equation is proposed to characterize the variations of E:

$$E = [\exp(f_{E0} S_T)]\left(v_1 E_T + v_2 E_{u\_p} \xi\right)\left\{\left[f_{E1}\left(\frac{1}{1+e}\right)^{f_{E2}\xi^{f_{E3}}}\right] \Big/ \left[1 + f_{E4}\left(\frac{e_0}{1+e_0}\right)\right]\right\} \tag{15}$$

where f_{Ei} is a fitting constant of the elastic modulus ($i = 0$–4); v_1 and v_2 respectively refer to the volume ratio of tailings and ultimate volume of cement paste relative to the total volume of the solid phase; E_T and E_{u_p} respectively represent the elastic modulus of the tailings, and the ultimate value of the elastic modulus of the cement paste at complete hydration; e and e_0 denote the void ratio and initial void ratio of the CPB, respectively. The variations in the void ratio e of CPB are controlled by the consolidation process. To predict the volume change and the resultant void ratio, Cui and Fall (2016c) developed a multiphysics model on the consolidation process which is incorporated into the present study. More details on this model can be found in (Cui and Fall 2015b, 2016c). The five fitting constants f_{Ei} can be obtained through a regression analysis on the experimental data of E from the UCS tests of the CPB considered. In this study, the experimental data reported by Fall et al. (2007) and Ghirian and Fall (2014) are used to determine the fitting constants. Correspondingly, $f_{E0} = -5.2$, $f_{E1} = 177.5$, $f_{E2} = 4.363$, $f_{E3} = -1.047$ and $f_{E4} = 3000$ are adopted in this study. Moreover, E_{u_p} can be determined by using a regression analysis on the experimental values of the elastic modulus of cement paste reported in (Janotka 2001; Lura et al. 2003; Ye et al. 2004). Correspondingly, $E_{u\_p} = 28.49$ GPa is obtained in this study. In addition, the volume ratio v_1 and v_2 can be derived from a previous study on CPB conducted by Cui and Fall (2015a):

$$v_1 = \frac{(1/C_m - 1)v_{tailings}}{(w/c)v_w + v_c + (1/C_m - 1)v_{tailings} - (2v_w - v_{ch-w} - v_{ab-w})R_{n-w/hc}\xi}$$

$$v_2 = \frac{\left[v_c + (v_{ch-w} + v_{ab-w})R_{n-w/hc}\right]\xi}{(w/c)v_w + v_c + (1/C_m - 1)v_{tailings} - (2v_w - v_{ch-w} - v_{ab-w})R_{n-w/hc}\xi} \quad (16)$$

With

$$R_{n-w/hc} = 0.187x_{C_3S} + 0.158x_{C_2S} + 0.665x_{C_3A} + 0.2130x_{C_4AF}$$

where v_w, v_c, $v_{tailings}$, $v_{ch\text{-}w}$ and $v_{ab\text{-}w}$ represent the specific volume (i.e., the inverse of density) of water, cement, tailings, chemically combined water and physically absorbed water, respectively. For the values of the specific volume, v_w, v_c, and $v_{tailings}$ are constant when the mixture recipe is determined. Moreover, a previous study on cement paste (Brouwers 2004) proved that $v_{ch\text{-}w} = 0.72$ cm^3/g and $v_{ab\text{-}w} = 0.90$ cm^3/g, and the specific volume of these two types of water does not change for all types of cement. $R_{n\text{-}w/n\text{-}whc.hc}$ refers to the mass fraction of the chemically combined water and hydrated cement, and x_i stands for the mass fraction of the clinker compositions of cement (i = C_3S, C_2S, C_3A and C_4AF). The good agreement ($R^2 = 0.85$) between the experimental values of the elastic modulus reported in (Ghirian and Fall 2016a; Wu et al. 2016), and prediction results (Fig. 4) validates the predictive ability of the elastic modulus (i.e., Eq. (15)) proposed in this study.

Apart from the elastic modulus E (see Eq. (15)), the Poisson's ratio υ is also important for determining the bulk modulus K_b. Previous experimental studies on the Poisson's ratio of CPB (Abdelaal 2011) and cement paste (Bittnar 2006; Boumiz et al. 1996) observed that both binder hydration and cement content can affect the changes in υ. Hence, the following predictive function is developed to describe the effect of the degree of binder hydration and cement content on υ:

$$\upsilon = 0.5\exp\left(N_{\upsilon 1}C_m^{N_{\upsilon 2}}\xi\right) + N_{\upsilon 3}\xi^{N_{\upsilon 4}}\exp\left(N_{\upsilon 5}C_m^{N_{\upsilon 2}}\xi^{N_{\upsilon 6}}\right) \quad (17)$$

where $N_{\upsilon i}$ denotes the fitting parameters (i = 1–6), which are influenced by the type of CPB. Based on a regression analysis on the measured υ reported in (Galaa et al. 2011), $N_{\upsilon 1} = -0.21$, $N_{\upsilon 2} = 0.02$, $N_{\upsilon 3} = -15000$, $N_{\upsilon 4} = 7$, $N_{\upsilon 5} = -11.66$ and $N_{\upsilon 6} = 0.7$ in the present study. Figure 5 shows that the measured values reported by Abdelaal (2011), Smilauer and Bittnar (2006) and Veenstra (2013) are well captured by the developed predictive function (Eq. (17)) and the coefficient of determination is 0.85.

To predict the CPB strength, four material parameters B_1, B_2, B_3 and B_4 in the hardening and softening parameters $\alpha(\xi, \kappa)$ should be determined as well. As already discussed in Sect. 3, the hardening/softening behavior of CPB becomes more obvious with curing time, which indicates that the four material parameters will change with the progression of binder hydration. To describe the effect of the binder hydration on the hardening/softening behavior, the following predictive functions developed by Cui and Fall (2016a) are adopted in this study.

$$\begin{aligned} B_1 &= R_{\alpha 1}\xi^{R_{\alpha 2}} + R_{\alpha 3} \\ B_2 &= R_{\alpha 4}\xi^{R_{\alpha 5}} + R_{\alpha 6} \\ B_3 &= R_{\alpha 7}\xi^{R_{\alpha 8}} + R_{\alpha 9} \\ B_4 &= R_{\alpha 10}\xi^{R_{\alpha 11}} + R_{\alpha 12} \end{aligned} \quad (18)$$

where $R_{\alpha i}$ is a fitting constant (i = 1–12) and depends on the type of CPB. $R_{\alpha 1} = -0.05$, $R_{\alpha 2} = 4.178$, $R_{\alpha 3} = 0.071$, $R_{\alpha 4} = -200$, $R_{\alpha 5} = 10$, $R_{\alpha 6} = 360.5$, $R_{\alpha 7} = 832.3$, $R_{\alpha 8} = 3$, $R_{\alpha 9} = 110$, $R_{\alpha 10} = 260.1$, $R_{\alpha 11} = 3.5$ and

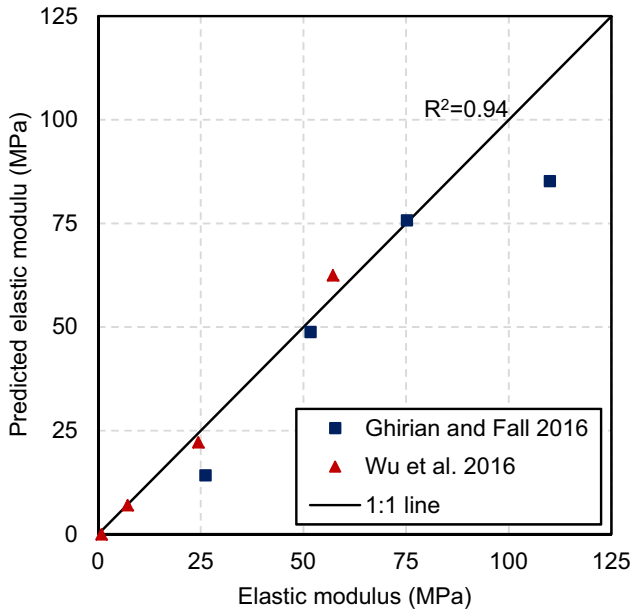

Fig. 4 Experimental versus predicted values of elastic modulus.

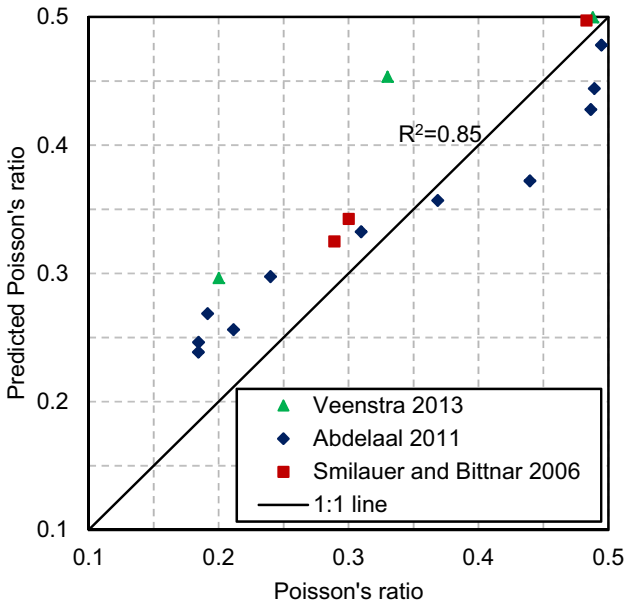

Fig. 5 Experimental versus predicted values of Poisson's ratio.

$R_{\alpha 12} = 80$, as suggested by Cui and Fall (2016a) are adopted in this study.

As discussed previously, the initial sulphate content in CPB can significantly affect the strength development in CPB mass. To capture its effect, the sulphide content, S_w, or the sulphate content, S_w, is incorporated into the predictive functions (Eqs. 13, 14 and 15) of material properties (i.e., cohesion c_B, internal friction angle ϕ_B, and elastic modulus E). The predictability of the proposed predictive functions has been validated by the good agreement between predicted results and reported experimental data (re: Figs. 2, 3, and 4). Meanwhile, the elastic modulus determines the rate of change of effective stress with respect to strain, and thus affects the stress level in CPB for a given strain value. Moreover, as indicated in Eq. (1), the cohesion c_B and internal friction angle ϕ_B dominate the shape of initial yield function (i.e., the initial strength without the contribution of strain hardening behavior). Therefore, through the incorporation of sulphate content into material properties, the effect of sulphate content on the CPB strength can be captured by this proposed multiphysics model.

5. Model Validation

To validate the predictive ability of the developed multiphysics model on CPB strength, a series of case studies were examined at both the laboratory and field scales. The developed model was implemented into a finite element method (FEM) code (Comsol, 2015). Moreover, to assess the sensitivity of the developed model to curing conditions including curing time and initial CPB temperature, the authors also performed a series of laboratory experiments including monitoring the temperature and suction changes in CPB and related measurements of UCS values of CPB with different curing times and initial temperatures.

It should be noted that there are two ways to apply the developed model on CPB strength. First, the multiphysics model on strength (i.e., Eq. (11)) can be directly used to predict CPB strength if the mixture recipe, PWP, pore-air pressure and temperature are given for the CPB samples. Otherwise, as already mentioned in Sect. 4 (i.e., Determination of Model Parameters), the fully coupled THMC model (Cui and Fall 2015a) and multiphysics model on consolidation (Cui and Fall 2016c) can be used to predict the pore pressure and temperature changes in CPB. In this study, the latter is adopted for the following case study and model application.

5.1 Case Study 1—Changes to CPB Strength with Different Initial Temperatures

Due to changes in geographical locations (e.g., warm to permafrost regions), underground mine depth, rock mass conditions and seasonal changes, the prepared fresh CPB may have different initial temperatures (Célestin and Fall 2009; Nasir and Fall 2010). Moreover, previous studies have shown that CPB strength can considerably change at the early ages (Belem et al. 2000; Fall et al. 2015). Therefore, to study the short-term changes in CPB strength under different initial temperatures, a laboratory monitoring and testing program is conducted in this study. For the laboratory experiment, CPB samples were prepared with three different initial temperatures of 5, 25, and 35 °C. The mixture recipe for preparing the CPB samples is provided in Table 1. The ground silica tailings were adopted to prepare CPB samples in this study. This is because (1) the silica tailings consist essentially of quartz, and thus the silica tailings will eliminate the uncertainties related to natural tailings (Ghirian and Fall 2015; Jiang et al. 2017); (2) moreover, quartz is one of the primary minerals found in Canadian hard-rock mine tailings (Aldhafeeri and Fall 2017; Cui and Fall 2015b), and thus it is reasonable to utilize silica tailings to study the CPB strength; (3) in addition, previous studies (Jiang et al. 2016; Wu et al. 2016) have demonstrated that the grain-size distribution of silica tailings is close to the average of nine Canadian hard-rock mine tailings.

After mixing, the fresh CPB with different initial temperatures was poured into a cylindrical mold (10 cm in diameter × 20 cm in height) in the laboratory. To imitate the slow rate of heat exchange between the CPB and rock mass in a stope (Wang and Fall 2014), a glass wool blanket with a thickness of 50 mm was used to cover the cylinder mold. The corresponding properties of the adopted thermal insulation material of the glass wool blanket are listed in Table 2.

Then, the CPB samples with different curing times (including 1, 3 and 7 days) were used to investigate the development of strength. When the target curing time was reached, the CPB samples were removed from the cylinder mold and trimmed into standard cylindrical specimens that were 50 mm in diameter and 100 mm in height. For trimming the CPB specimens, the jigsaw blade was first adopted to cut the bases of the samples. Then, the final test specimens were obtained using a utility knife and an adjustable sample trimmer to scrape the curved face of the CPB specimens. In addition, to ensure the precise diameter and height of cylindrical specimens, a digital fractional caliper was employed during the trimming process. Then, UCS testing was performed on them in accordance with ASTM C39. To ensure the repeatability of the testing results, three samples were tested for each curing time and each initial temperature. Meanwhile, to further study the changes in strength and related influential factors, the suction and temperature changes were monitored (see Fig. 6). Specifically, suction meters (Model: MPS-2; Decagon) and temperature sensors (Model: 5TE; Decagon) were adopted to record the suction and temperature changes in the CPB samples.

The developed model was then implemented in COMSOL to predict the CPB strength, and an axisymmetric geometry model was adopted to represent the cylindrical mold and thermal insulation material (see Fig. 7). The adopted initial values and boundary conditions are provided in Table 3.

A comparison of the predicted CPB strength and measured values is presented in Fig. 8. It can be observed that (1) as expected, the curing time plays a significant role in changes to the CPB strength. As the curing time increases, a higher value of the strength is obtained, mainly because, as

Table 1 Mixture recipe for preparation of CPB samples.

Cement type	Cement content (wt %)	Mixing water	W/C ratio	Tailings type	Mixing time (mins)
Portland cement type I	4.5	Tap water	7.6	Ground silica tailings	7

wt% weight percentage of cement to total solid weight; *W/C ratio* water-to-cement ratio.

Table 2 Properties of thermal insulation material.

Thermal conductivity (W/m·K)	Heat capacity (J/kg·K)	Density (kg/m^3)
0.035	840	30

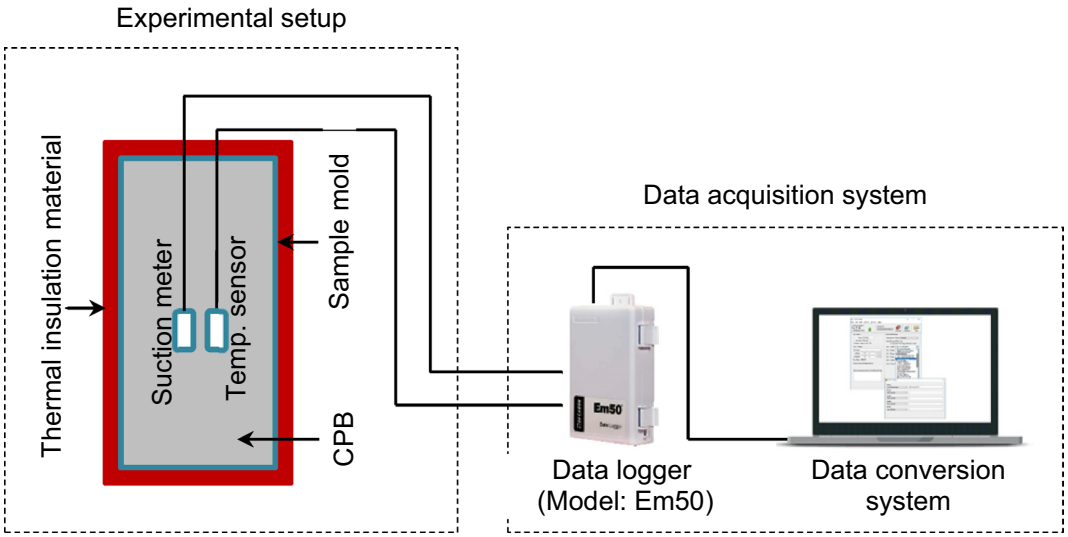

Fig. 6 Schematic diagram of experimental setup to test CPB strength under different initial temperatures.

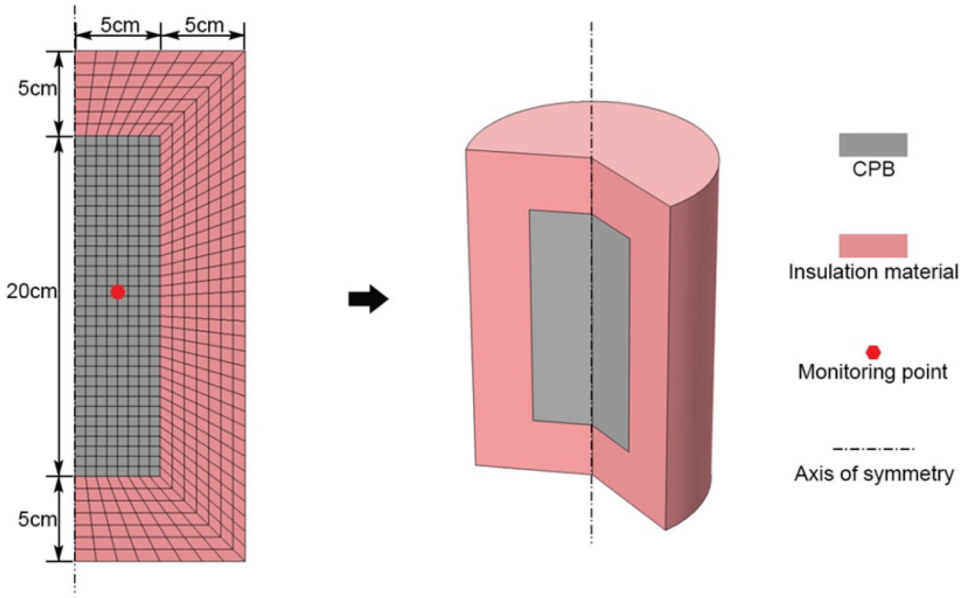

Fig. 7 Mesh and geometry of simulated cell test.

mentioned earlier, the bonding strength will progressively improve with the precipitation of the hydration products between the tailings particles. Consequently, CPB strength demonstrates an increasing trend with curing time. However, it should be noted that the time rate of change of CPB strength decreases with curing time, which is attributed to the decrease in the rate of hydration with curing time. In this regard, the PWP changes (Fig. 9a) in the CPB can further prove the reduction of the rate of binder hydration with time. As can be seen in Fig. 9a, both the simulated and monitored PWP demonstrate a reduction with curing time. However, the rate of change of the PWP (i.e., the curved slope) becomes smaller with time. Since water drainage and evaporation on the top surface of the CPB sample are not

Table 3 Initial values and boundary conditions in Case Study 1.

Parameter	Value
Mechanical component	
Top surface	Free
Lateral sides	Roller
Bottom side	Fixed
Volume force	Gravity
Hydraulic component	
Surrounding surfaces	No flow
Volume force	Gravity
Initial value	Hydraulic head = 0
Thermal component	
Surrounding surfaces (°C)	22
Initial temperature (°C)	5, 25 and 35

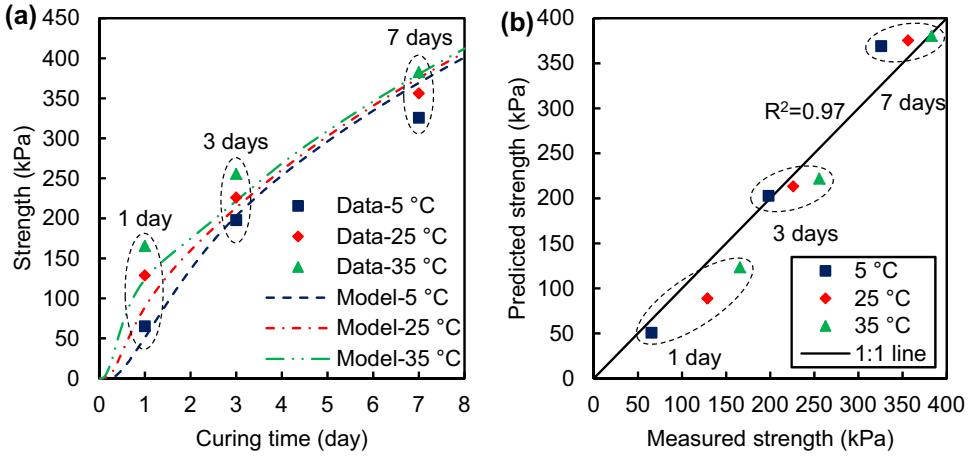

Fig. 8 Comparison of predicted results and experimental values of true CPB strength: **a** changes to CPB strength with curing time and **b** correlation between simulated results and measured values.

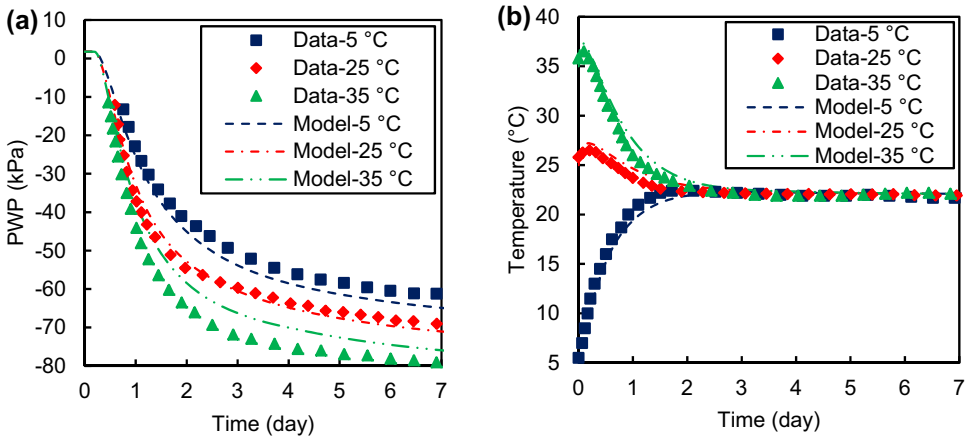

Fig. 9 Comparison of predicted results and experimental values: **a** PWP and **b** temperature.

allowed in this cell test, the resultant variation of the PWP in the CPB sample is controlled by the pore-water consumption caused by binder hydration (i.e., self-desiccation process). Therefore, the changes in the PWP are directly associated with the variations in the rate of hydration in the CPB, namely a decrease in rate of hydration occurs with curing time, (2) both the simulated results and measured values indicate that the initial CPB temperature can affect the CPB

strength, especially at the very early ages. This is due to the temperature dependence of the rate of binder hydration (Cui 2017; Cui and Fall 2017c). Specifically, the different initial temperatures can significantly affect temperature changes in CPB samples at the very early ages (especially the first 2 days, see Fig. 9b). Correspondingly, the resulting degree of hydration of the CPB samples with different initial temperatures differs. As a result, a higher temperature can accelerate the development of binder hydration, and thus generate more hydration products (Nasir and Fall 2010; Wu et al. 2013). Therefore, higher CPB strength is observed in CPB with a higher initial temperature. In addition, as shown in Fig. 9b, the temperature in all of the CPB samples gradually approaches room temperature (i.e., 22 °C) after approximately two-days of curing. Correspondingly, as indicated in Fig. 8a, the difference in CPB strength becomes smaller with reduced temperature differences. However, due to the contribution of the PWP to the CPB strength (see Fig. 9a), there is still a small difference in the CPB strength among the CPB samples at the same room temperature even after two-days of curing, (3) it can be found that in Fig. 8b, the changes to the CPB strength can be well captured by the developed model on strength (the coefficient of determination is 0.97). Therefore, the developed model can be used to predict the development of CPB strength with different curing times and initial temperatures.

5.2 Case Study 2—Changes to CPB Strength with Different Sulphate Contents

Due to the inhibition of cement hydration by sulphate ions (Li and Fall 2016), previous experimental studies (e.g., Ercikdi et al. 2009; Fall and Benzaazoua 2005) on CPB have observed that the sulphate content in the mixing water has a significant effect on the development of CPB strength. To further validate the developed model for CPB materials with different sulphate contents, the experimental data reported in (Li and Fall 2016) were collected and then compared with the predicted results. The adopted mixture recipe and the design of the testing program for this experimental study are provided in Tables 4 and 5, respectively.

Simulation with the developed model was carried out based on the design of the testing program. An axisymmetric geometry model was adopted to simulate the CPB sample (see Fig. 10), and the adopted initial values and boundary conditions were the same as those in Case Study 1.

Figure 11 is a comparison between the predicted results and measured values of CPB strength with different sulphate contents. As shown in Fig. 11a, both the simulated results and measured values indicate that the sulphate content can significantly affect CPB strength. Specifically, with an increase in the sulphate content in the mixing water, the negative effects on CPB strength become more obvious. For example, compared with the values of CPB strength (677 kPa) obtained from the CPB control sample (i.e., sulphate content = 0 ppm) with a curing time of 28-days, the predicted CPB strength respectively reduces to 619 kPa for 5000 ppm of sulphate, 517 kPa for 15,000 ppm, and 431 kPa for 25,000 ppm. As mentioned, the reduction in CPB strength with increased sulphate content is due to the inhibition of the binder hydration by the sulphate ions. In addition, as can be seen in Fig. 11b, an excellent agreement ($R^2 = 0.98$) is obtained between the experimental values and predicted results. Therefore, the developed model is able to determine the effects of sulphate content on the development of CPB strength for the curing times considered in this study (up to 28 days).

In addition, based on previous studies (Cihangir et al. 2012, 2015) on the effect of sulphate content on CPB strength, a strength loss was observed in CPB with long-term curing period due to the acid and sulphate attack. As shown in Fig. 11a, the adverse effect of sulphate content on CPB strength was considered in this proposed model. However, it should be noted that the long-term adverse effect of sulphate content on CPB strength (i.e., the strength loss phenomenon) was not incorporated in this study. This effect should be included in future model developments.

5.3 Case Study 3—Long-Term Strength of CPB with Various Cement Contents

As per the requirements of CPB design for mechanical stability and cost management, the binder content adopted in a backfilled stope may differ from one to another. To study the effects of cement content on the changes to CPB strength, extensive laboratory experiments have been carried out (Ercikdi et al. 2014; e.g., Fall et al. 2008). Therefore, to validate the predictive ability of the developed model for CPB with different cement contents, the laboratory experiment conducted by Belem et al. (2000) and the reported data are adopted in this study. Three different weight percentages of cement (including 3, 4.5 and 6 wt%) were considered in Belem et al. (2000). Details on the mixture recipe and the testing program are provided in Tables 6 and 7, respectively.

It should be noted that, in this experiment, the fresh CPB was first poured into a sample mold with a diameter of 10 cm and height of 20 cm. Then, the CPB sample was taken out and trimmed into standard specimen size (5 cm (D) × 10 cm (H)) for UCS testing. Therefore, an axisymmetric geometry is used to simulate the CPB sample (see Fig. 12). The same boundary conditions as those of Case Study 1 are adopted.

Table 4 Mixture recipe in Case Study 2.

Sulphate type	Sulphate concentration (ppm)	Cement content (wt%)	Cement type	Tailings type	W/C ratio
Ferrous sulphate ($FeSO_4 \cdot 7H_2O$)	0, 5000, 15,000 and 25,000	4.5	Portland cement type I	Silica tailings	7.6

wt% weight percentage of cement to total solid weight; *W/C ratio* water-to-cement ratio.

Table 5 Testing program in Case Study 2.

Curing time (days)	Testing time (days)	Curing temperature (°C)	Sample size (cm)
28	1, 3, 7, and 28	22	5(D) × 10(H)

D diameter, *H* height.

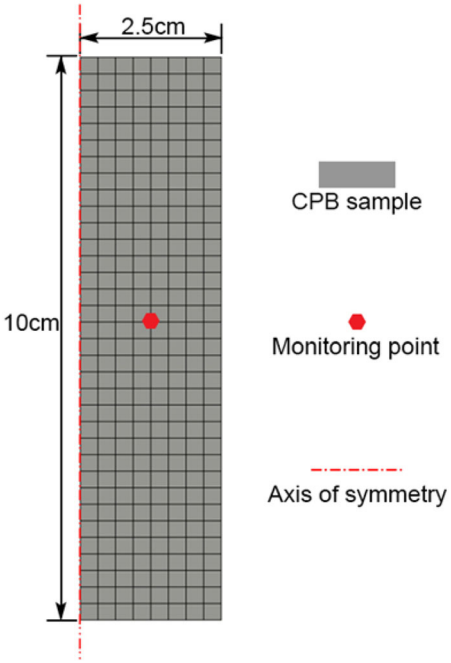

Fig. 10 Mesh and geometry of simulated CPB sample for Case Study 2.

A comparison between the predicted results and experimental values of CPB strength is presented in Fig. 13. As can be seen in Fig. 13a, the developed model on CPB strength is sensitive to the changes in cement content. For instance, compared with the predicted strength (410 kPa) of CPB with a cement content of 3% and curing time of 91-days, the simulated CPB strength is increased by approximately 50% for a cement content of 4.5% (strength = 616 kPa), and by around 100% for a cement content of 6% (strength = 821 kPa). Therefore, the developed model can simulate the improvements in CPB strength with increased cement content. Moreover, it is apparent by looking at Fig. 13a that the time rate of change of CPB strength decreases with curing time regardless of the cement content, which is consistent with the findings obtained in Case Study 1. The reason has been discussed earlier. In addition, the good agreement between the simulated results and measured values (see Fig. 13b) proves the predictive ability of the developed model for long-term CPB strength with different cement contents.

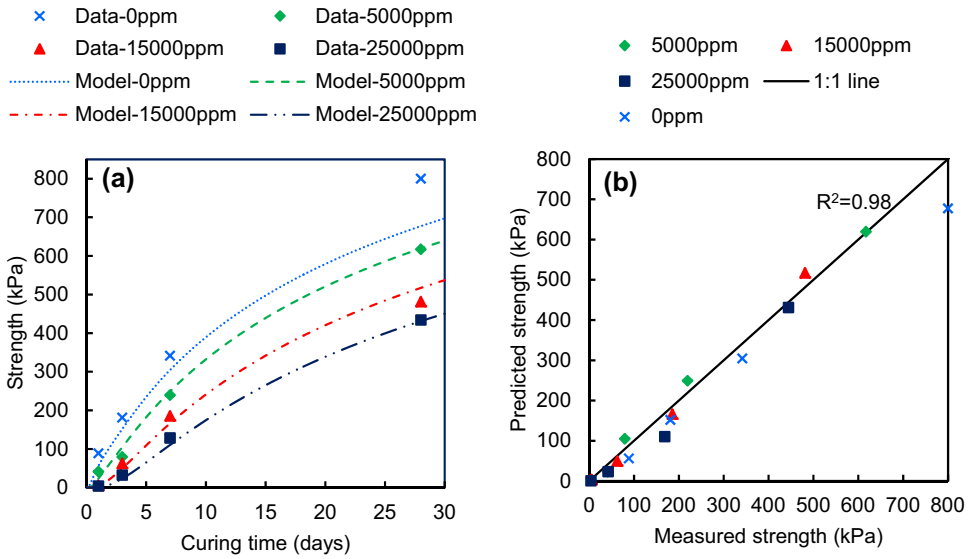

Fig. 11 Effect of sulphate content on CPB strength: **a** changes to CPB strength with curing time and **b** correlation between predicted results and measured CPB strength values.

Table 6 Mixture recipe adopted in Case Study 3.

Cement type	Cement content (wt%)	W/C ratio	Tailings type	Sulphur content of tailings (wt%)
Portland cement type I	3, 4.5, and 6	12, 8, and 6	Tailings from metal mine	16

wt% weight percentage of cement to total solid weight; *W/C ratio* water-to-cement ratio.

Table 7 Testing program in Case Study 2.

Curing time (days)	Testing time (days)	Curing temperature (°C)	Sample size (cm)
112	14, 28, 56, 91, and 112	22	10(D) × 20(H)

D diameter, *H* height.

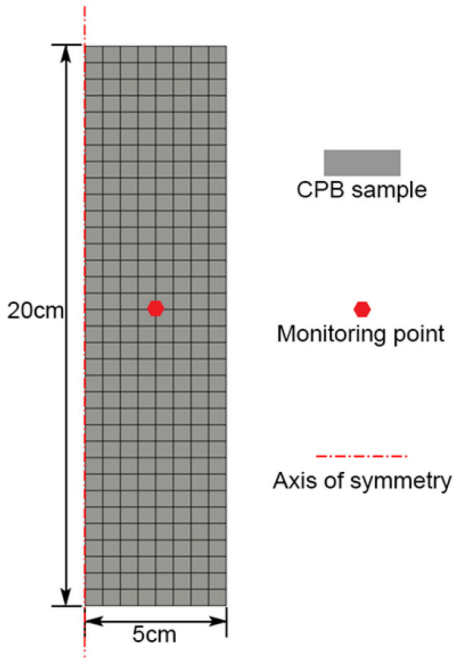

Fig. 12 Mesh and geometry of simulated CPB sample in Case Study 3.

6. Model Application

As demonstrated in Sect. 5, the developed model is able to evaluate the changes to CPB strength with different curing ages and mixture recipes in a satisfactory manner. Therefore, a series of engineering applications with the model are carried out in this section to investigate the changes in CPB strength in the field under various conditions, including different stope geometries, inclination angles, backfilling strategies and filling rates. The adopted initial values and boundary conditions are listed in Table 8.

Moreover, a control stope with dimensions of 8 m (W) × 16 m (H) was used as a reference. The barricade structure (4 m (W) × 4 m (H)) is located at the base of the stope (see Fig. 14). All of the numerical investigations were carried out by specifically modifying the control stope. The monitored point is located at the bottom of the stope. Moreover, to demonstrate the influence of the fill height on changes to the CPB strength, the middle of the CPB mass (i.e., 8 m away from the stope base) was examined, and a relevant discussion is presented in Sect. 6.1.

In addition, it should be noted that the investigated CPB strength in the following subsection refers to the "true" CPB strength, namely the effects of coupled THMC processes that occur in CPB are fully considered.

6.1 Effect of Stope Size

Due to the different stoping methods and mining plans, the stope geometrical size may vary from one stope to another. To investigate the effect of stope geometry on the development of CPB strength, a range of stope sizes: 5 m (W) × 10 m (H), 8 m (W) × 16 m (H), and 10 m (W) × 20 m (H), are considered in this study. Moreover, the same filling strategy (i.e., filling in two stages with 1-day plug), filling rate (0.5 m/h), barricade size, boundary and initial boundary conditions (see Table 8) are adopted for these three investigated stope sizes.

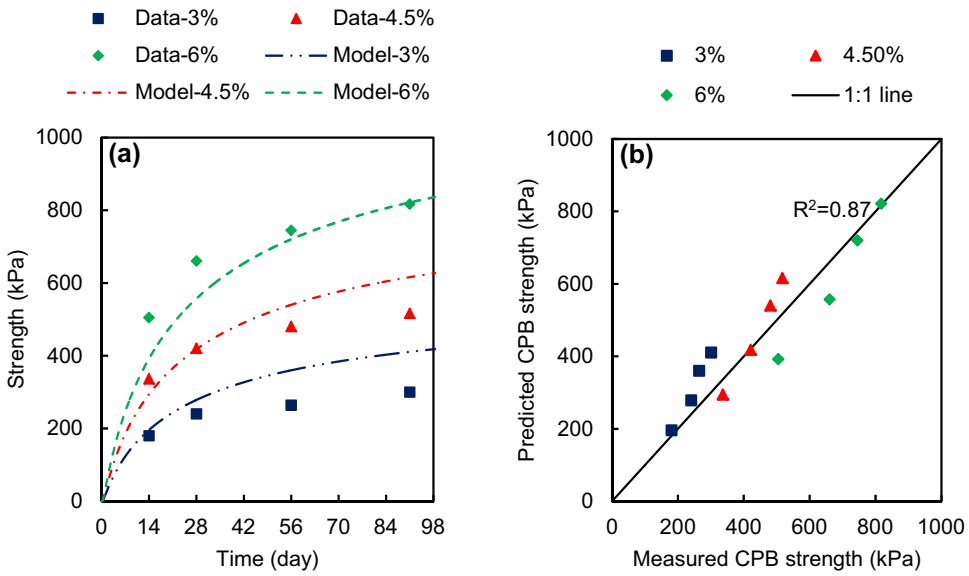

Fig. 13 Effect of cement content on long-term CPB strength: **a** changes to CPB strength with curing time and **b** correlation between predicted results and measured CPB strength values.

Table 8 Input parameters, initial values and boundary conditions of control CPB and rock mass.

Parameter	Value
Backfill	
Stope size (m)	8(W) × 16(H)
Barricade size (m)	4(W) × 4(H)
Stope inclination angle (°)	90
Cement content (wt%)	Residual fill: 4.5, and plug fill: 7
w/c ratio	7.6
Initial void ratio	1
Filling rate (m/h)	0.5
Filling strategy	2-stages with 1-day plug
Rock mass	
Density (kg/m^3)	2500
Young's modulus (GPa)	30
Poisson's ratio	0.3
Thermal conductivity (W/m·K)	3.9
Heat capacity (J/Kg·K)	790
Mechanical component	
Top surface	Free
Lateral sides	Roller
Bottom side	Fixed
Volume force	Gravity
Hydraulic component	
Surrounding surfaces	No flow
Volume force	Gravity
Initial value	Hydraulic head = 0
Thermal component	
Surrounding surfaces (°C)	25
Initial temp. (°C)	25

Figure 15 shows the effect of the stope size on the strength development in CPB. The CPB strength is represented with normalized strength (i.e., CPB strength at any time/CPB strength obtained for 160-day CPB). Here, it is assumed that after 160 days, there is no significant increase in CPB strength with curing time, namely, the 160-day strength is the ultimate CPB strength. From Fig. 15, it can be clearly seen that (1) CPB strength along the center line of the stope is higher relative to that near the surrounding rock walls, which is consistent with the findings in a previous study on CPB strength (Nasir and Fall 2010). Moreover, the non-uniform distribution of CPB strength becomes more obvious with time. This is partly because of the PWP changes in the CPB due to the self-desiccation process. With progression of pore-water consumption caused by binder hydration, and water drainage through the barricade, the PWP will change with time and thus affect the development of the CPB strength. Moreover, as discussed earlier in Case Study 1, the CPB strength is sensitive to variations in temperature. The temperature changes are determined by the heat transfer between the CPB and rock mass, and heat generated by binder hydration. As a result, the changes in temperature can further contribute to non-uniform distribution of CPB strength in fill mass. (2) The stope size has a significant effect on the development of CPB strength. Specifically, higher strength is obtained in a larger stope at a given curing age, which is consistent with the results of previous study on CPB strength (Nasir and Fall 2010). This is mainly attributed to more heat generated within larger CPB mass, which can further leads to the increase in temperature, and thus the development of CPB strength.

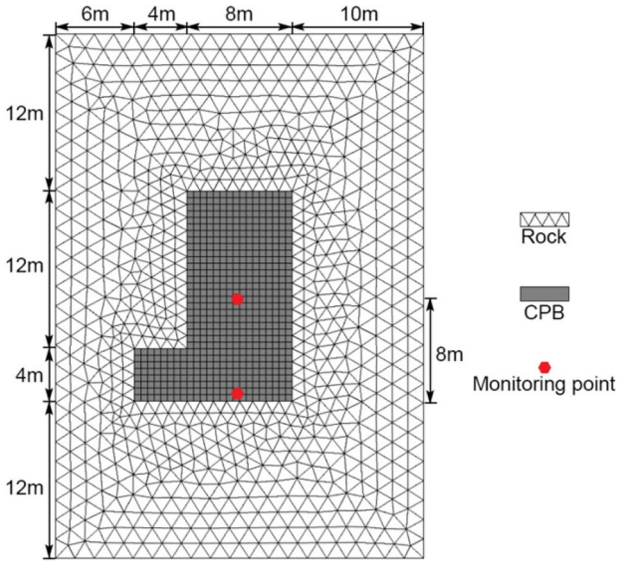

Fig. 14 Mesh and geometry of control stope.

However, it should be noted that the effect of stope size on the strength is also a function of the binder content of the CPB considered. For low binder content, Fig. 16 reveals that the strength for smaller stope is higher than the strength of larger stope (higher height). This is because with the decrease in binder content, the amount of heat released by binder hydration will be reduced, which, in turn, weakens the effect of thermal process on the development of CPB strength. Moreover, the pore-water loss induced by binder hydration (i.e., self-desiccation process) decreases with a reduction of the binder content. Consequently, smaller stope with lower total stress can result in higher effective stress with respect to similar changes in PWP. Therefore, higher strength is observed in small stope with the decrease of cement content. Therefore, the obtained results further verify that a reliable evaluation of in situ CPB strength requires an evaluation of the multiphysics processes in the field (i.e., the modelling and simulation of field behavior of CPB).

Moreover, to demonstrate the effect of the fill height on the variations in CPB strength, a comparison of the prediction results at the bottom and middle of the control CPB mass is plotted in Fig. 17. The obtained results indicate that (1) at the very early ages, higher strength is formed at the bottom of the CPB mass compared to the middle of the CPB mass. This is because relatively fresh CPB is found higher on the filled stope due to the backfilling operation which is continuous or done by sequences. As a result, CPB found lower on the filled stope requires a longer curing time compared to that found higher on the stope. Hence, binder hydration can advance more at the bottom of the CPB, which contributes to the further enhancement of CPB strength; (2) after around 4-days of curing, the CPB strength at the middle of the CPB mass progressively increases as opposed to that at the bottom of the CPB mass. This can be attributed to the dissipation of the PWP caused by water drainage through the barricade and water consumption caused by binder hydration. With pore-water loss, a lower PWP appears at the middle of the CPB mass and thus contributes to the improvement of the CPB strength to a larger extent. Therefore, greater CPB strength gradually develops in the middle of the CPB mass with curing time.

6.2 Effect of Inclination Angles of Stope

Due to influence of ore bodies, the resultant stopes may have various inclination angles (Cui and Fall 2017c; Li and Aubertin 2009). Hence, the effect of inclined stopes on strength development is investigated in the present study. The inclination angles of the control stope were respectively set to 90°, 70° and 50°. Figure 18 shows the prediction results of CPB strength for these three inclination angles. It can be seen that the inclination angle has a very limited effect on the changes in CPB strength. However, for the spatial distribution of CPB strength (see Fig. 19), inclined stopes (i.e., Figure 19a, b) can form a larger area with higher CPB strength compared to a vertical stope (Fig. 19c).

6.3 Effect of Backfilling Strategy

Due to the differences in mining operations, CPB recipe and stope geometry, the adopted filling strategy (i.e., continuous filling or filling carried out in stages) may vary from one site to another in backfilling practices (Veenstra et al. 2011). For instance, filling operations carried out in two stages with a plug layer cured for 1 day or more are commonly adopted (Ghirian and Fall 2013). The adopted backfilling strategy can directly affect filling time and thus mine cycle and productivity. Therefore, it is important to investigate the effect of the filling strategy on the development of early strength of CPB. In this study, both continuous filling and filling carried out in stages with 1- and 2-day plug layers are respectively investigated in the control stope. For these three cases, the adopted filling rate is 0.5 m/h. A comparison of the development of early-age strength in the control stope with the different filling strategies is presented in Fig. 20. It can be observed that a higher CPB strength is obtained in the plug layer with longer curing time. Specifically, the plug normalized strength reaches approximately 3 and 9% for the 1- and 2-day plug layers, respectively, while there is no significant development of CPB strength for the continuous filling case. This is because filling operations carried out in stages allow a longer curing time of the CPB in the stope. Therefore, the binder hydration, heat transfer between the CPB and rock mass, water loss caused by the self-desiccation process and water drainage through the barricade are increased. Consequently, a higher CPB strength can be realized with filling operations carried out in stages with a longer curing time of the plug layer. The lower CPB strength at the early-ages associated with continuous filling could increase the cost of the barricade structure and the risk of CPB liquefaction (Abdelaal 2011), so improving CPB strength with a longer curing time of the plug layer is important for CPB stability. However, it should be noted that the filling operations carried out in stages with longer curing time of the plug layer will increase the total filling time and thus affects the mining cycle.

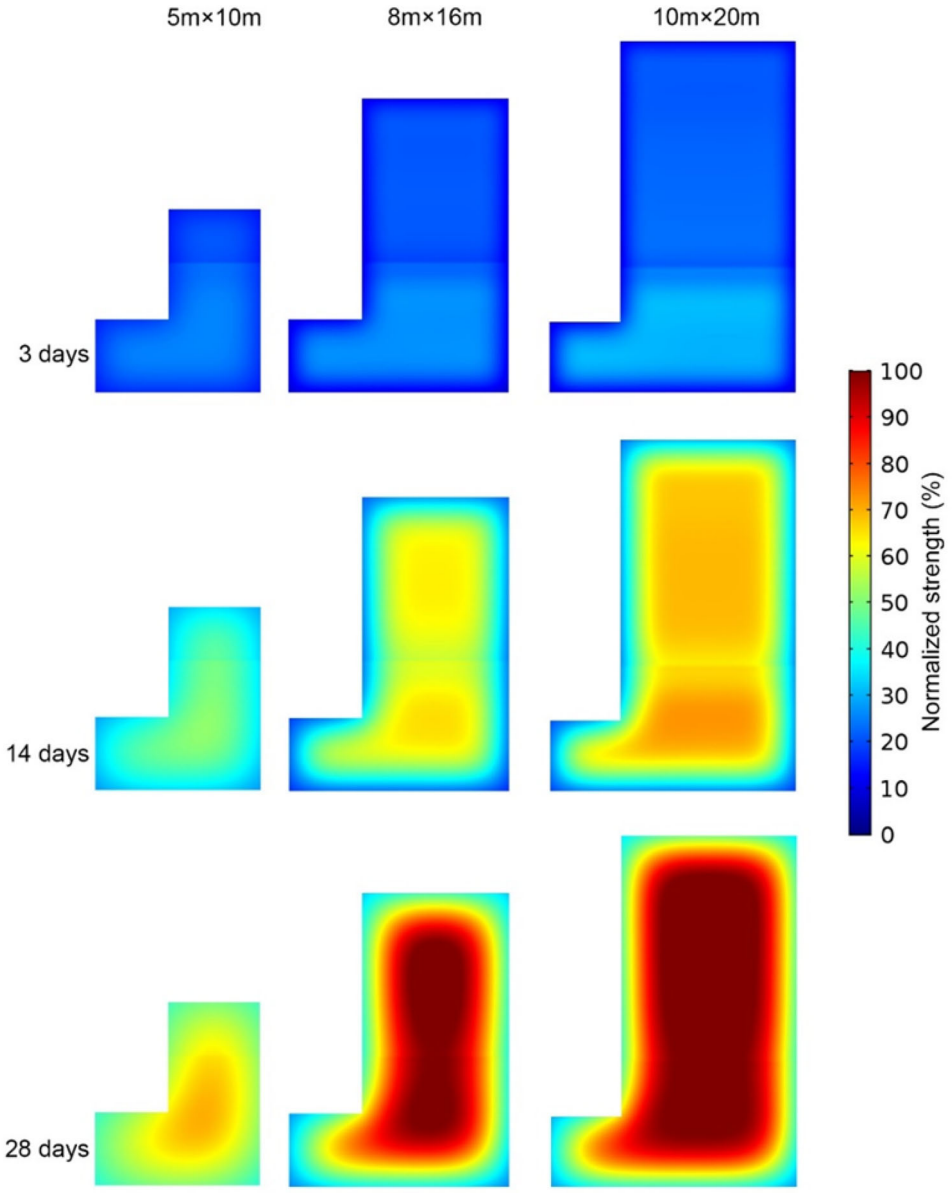

Fig. 15 Effect of stope size on spatial distribution of the strength CPB with higher binder content (Cement content 100 kg/m^3 i.e., 9.6 wt%).

6.4 Effect of Filling Rate

Apart from the filling sequences, the backfilling rate is another important factor which should be considered during CPB design. Changes in filling rates may result in different curing times for CPB material and thus affect CPB strength. In addition, similar to filling strategies, the filling rate also affects the mining cycle and productivity (Veenstra et al. 2011). Therefore, an investigation of filling rates (including 1, 0.5 and 0.25 m/h) on the development of CPB strength is carried out in this study. A comparison of the CPB strength in a stope subjected to different filling rates is shown in Fig. 21. It can be seen that, as expected, higher early-age strength is obtained in CPB with a slower filling rate. For example, after the rest period of the plug layer (i.e., 31 h for 1 m/h, 38 h for 0.5 m/h and 52 h for 0.25 m/h), the normalized CPB strength reaches approximately 1, 3 and 7%, respectively. Moreover, similar to the filling strategy, the effect of the filling rate also has significant impacts on the spatial distribution of early-age strength in the control stope (see Fig. 22). As shown in Fig. 22, higher CPB strength is formed with reduced rate of filling. This is because as discussed previously, slow backfilling process can result in longer curing time for a given filling height, and thus contribute to the development of CPB strength. As a result, the ability of a CPB structure to resist potential failures (e.g., barricade failure or CPB liquefaction) can be much improved.

7. Conclusions

In this study, a multiphysics model on CPB strength is developed to numerically simulate the development of CPB strength under the influence of coupled THMC processes. This developed model on CPB strength is coupled with a THMC model (Cui and Fall 2015a) and a multiphysics

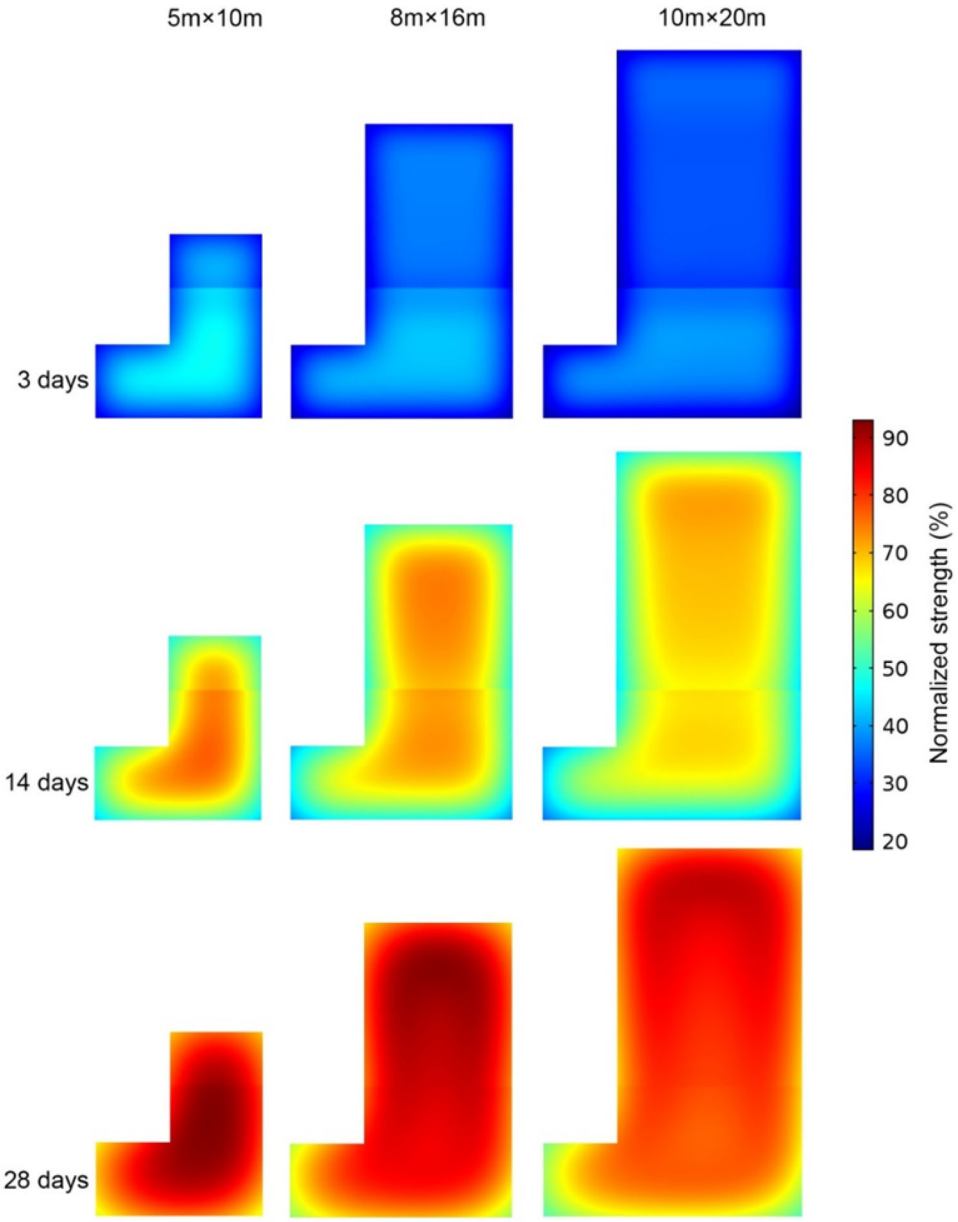

Fig. 16 Effect of stope size on spatial distribution of the strength of CPB with lower binder content (Cement content 60.358 kg/m^3 i.e., 4.5 wt%).

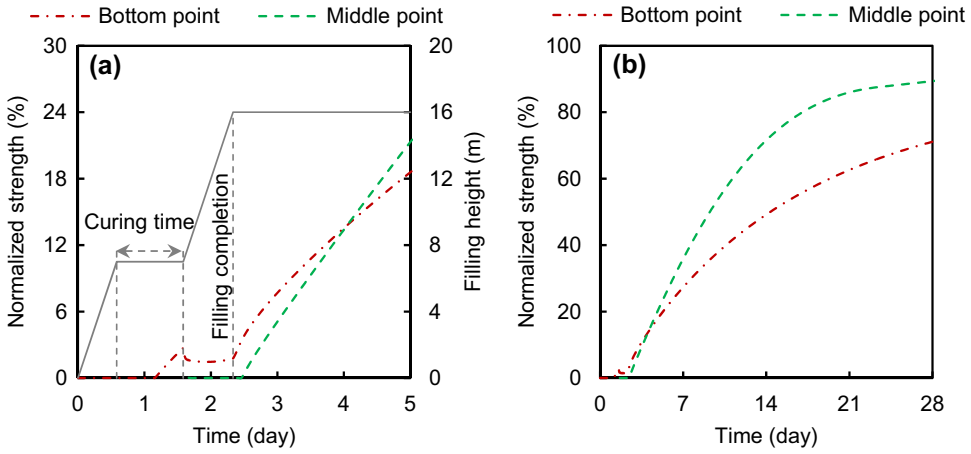

Fig. 17 Effect of fill height on PWP changes at bottom of CPB mass: **a** filling stage and **b** post-filling stage.

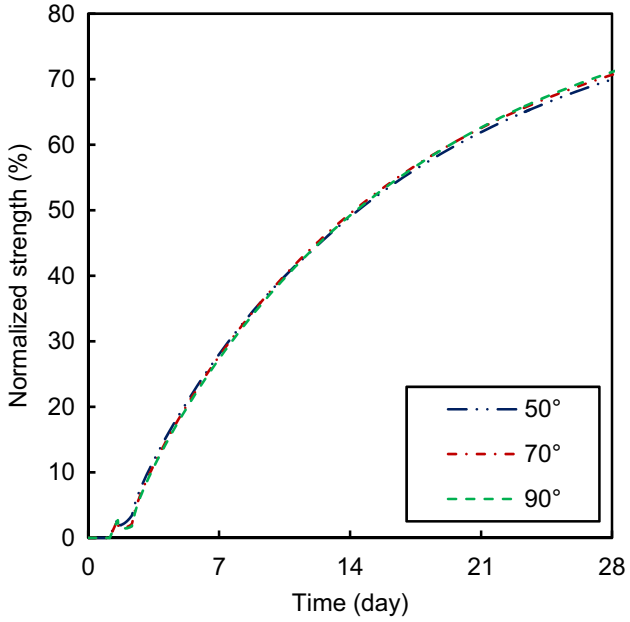

Fig. 18 Effect of inclination angle on changes to CPB strength at the bottom of CPB mass.

model on consolidation (Cui and Fall 2016c). Moreover, the effect of binder hydration, mixture recipe, tailings and mixing water (i.e., sulphate content) are fully considered for determining the material properties. The related model coefficients are determined with measurable parameters.

To validate the proposed model, the authors performed a laboratory monitoring and testing program to study the effects of the initial temperature on CPB strength. The good agreement between the prediction results and experimental values confirms the feasibility of the developed model. In addition, the model is further validated against experimental data reported in the literature. The results demonstrate not only the accuracy of the model for predictions, but also its sensitivity to the CPB temperature and mixture recipe (including the sulphate contents in the mixture water and cement content).

In terms of the model application, the obtained results demonstrate that the stope size, backfilling strategy and filling rate can significantly affect the development of in situ CPB strength. Moreover, the inclination angle has little influence on the amount of CPB strength. In addition, the

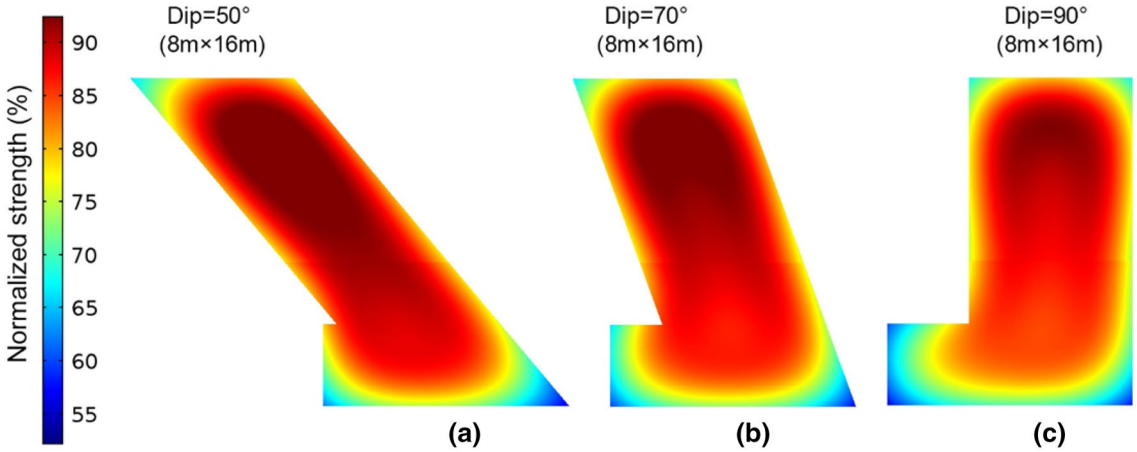

Fig. 19 Effect of inclination angle on spatial distribution of strength of CPB with curing time of 28-days: **a** 50°, **b** 70°, and **c** 90°.

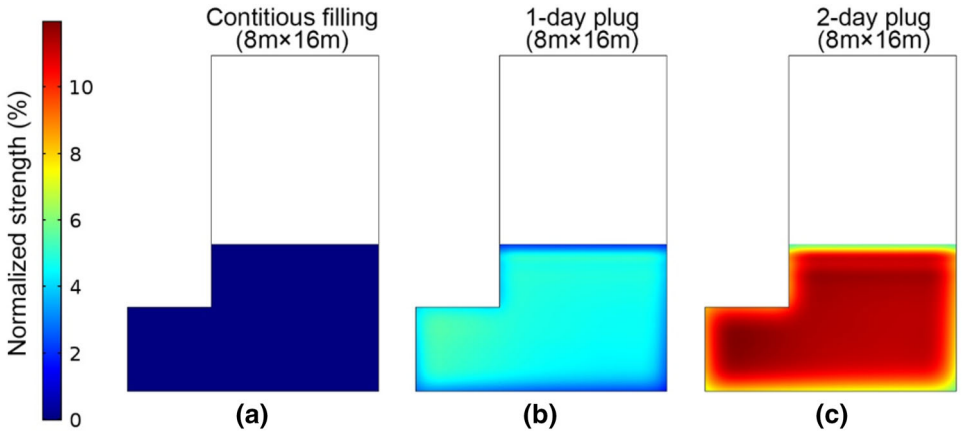

Fig. 20 Effect of filling strategy on spatial distribution of early-age strength of CPB after curing of plug layer: **a** continuous filling, **b** 1-day plug, and **c** 2-day plug.

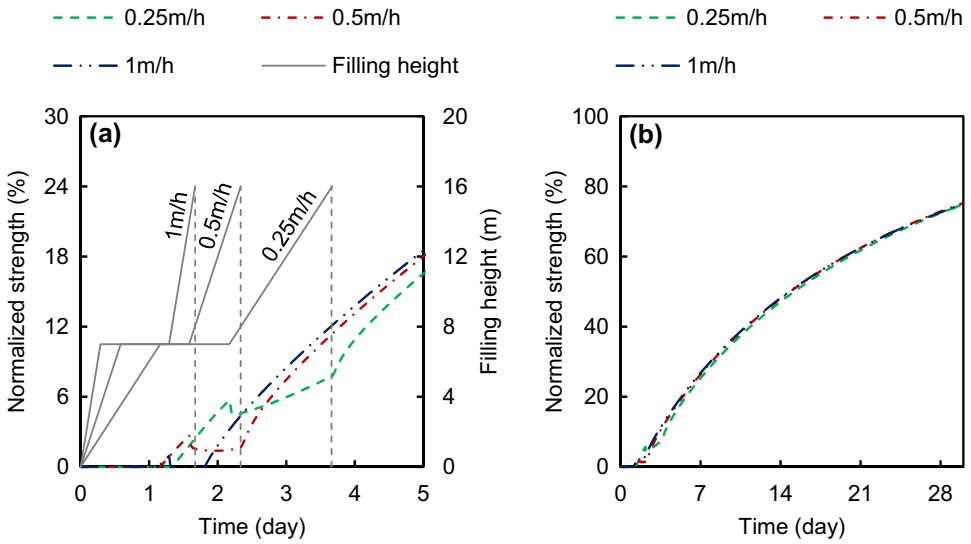

Fig. 21 Effect of filling rate on changes to CPB strength: **a** filling stage and **b** post-filling stage.

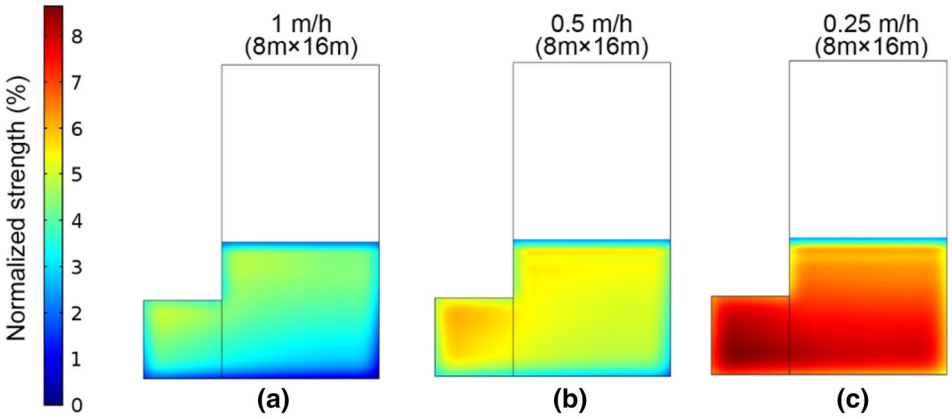

Fig. 22 Effect of filling rate on spatial distribution of early-age strength of CPB after curing of plug layer: **a** 1 m/h, **b** 0.5 m/h, and **c** 0.25 m/h.

developed model can well capture the effect of filling rate on the development of early-age strength in fill mass. Therefore, the developed multiphysics model on CPB strength can be used as a useful tool for an optimal design of CPB structures and reliable analysis of their mechanical stability.

Open Access

This article is distributed under the terms of the Creative Commons Attribution 4.0 International License (http://creativecommons.org/licenses/by/4.0/), which permits un restricted use, distribution, and reproduction in any medium, provided you give appropriate credit to the original author(s) and the source, provide a link to the Creative Commons license, and indicate if changes were made.

Appendix A. Determination of Coefficient κ_s

First, the 3-term exponential Eq. (8) can rewritten as:

$$B_2 \exp(-B_2\kappa_s) + B_3 \exp(-B_4\kappa_s) = B_3B_4\kappa_s \exp(-B_4\kappa_s) \tag{A.1}$$

Take the natural logarithm (i.e., ln) of both sides

$$\ln B_2 - B_2\kappa_s + \ln B_3 - B_4\kappa_s = \ln(B_3B_4) + \ln \kappa_s - B_4\kappa_s \tag{A.2}$$

Namely,

$$\ln B_2 + \ln B_3 - \ln(B_3B_4) = \ln \kappa_s + B_2\kappa_s \tag{A.3}$$

Apply the natural logarithm property

$$\ln\left(\frac{B_2}{B_4}\right) = \ln \kappa_s + B_2\kappa_s \tag{A.4}$$

Then, take exponential of both sides

$$\frac{B_2}{B_4}\exp(-B_2\kappa_s) = \kappa_s \tag{A.5}$$

To derive a closed-form solution to Eq. (A.5), Taylor series expansion is applied to the exponential term (i.e., exp (− $B_2\kappa_s$)):

$$\exp(-B_2\kappa_s) = 1 + (-B_2)x + B_2^2x^2/2 \tag{A.6}$$

Then, Eq. (A.5) can be transformed into a quadratic polynomial by substituting Eq. (A.6) into Eq. (A.5):

$$B_2^3\kappa_s^2 - 2\left(B_2^2 + B_4\right)\kappa_s + 2B_2 = 0 \tag{A.7}$$

Then, the solution to the second-order polynomial Eq. (A.7) can be derived by using quadratic formula:

$$\kappa_s = \frac{\left(B_2^2 + B_4\right) \pm \sqrt{B_4^2 + B_2^2B_4 - B_2^4}}{B_2^3} \tag{A.8}$$

It should be pointed out that the discriminant term (i.e., the square-root part of Eq. (A.8)) is greater than zero based on the allowed range of values of B_2 and B_4 (see Eq. (18)). Moreover, based on the definition of cumulative plastic strain κ_s, the solution with "plus" discriminant is adopted to determine the cumulative plastic strain corresponding to the peak stress (i.e., the nominal CPB strength).

$$\kappa_s = \frac{B_2^2 + B_4 + \sqrt{B_4^2 + B_2^2B_4 - B_2^4}}{B_2^3} \tag{A.9}$$

Appendix B. Fully Coupled THMC Model

The fully coupled THMC model (Cui and Fall 2015a) consists of four conservation equations:Pore-water mass balance equation:

$$\begin{aligned}
&\phi S\frac{\partial\rho_w}{\partial t} + \phi\rho_w\frac{\partial S}{\partial t} + S\rho_w\left[\frac{\partial\varepsilon_v}{\partial t} + \frac{(1-\phi)}{\rho_s}\frac{\partial\rho_s}{\partial t}\right] \\
&- \nabla\cdot\left(\phi S\rho_w k\frac{k_{rw}}{\mu_w}\nabla(P_w - \rho_w g)\right) = \phi S\left(\frac{\rho_w}{\rho_s}S - 1\right) \\
&\times\{2m_{hc0}(0.187x_{C_3S} + 0.158x_{C_2S} \\
&+ 0.665x_{C_3A} + 0.2130x_{C_4AF}) \\
&\times\left\{\left(\frac{\tau}{t_e}\right)^{\beta}\left(\frac{\beta}{t_e}\right)\xi\exp\left[\frac{E_a}{R}\left(\frac{1}{273+T_r} - \frac{1}{273+T}\right)\right]\right\}\}
\end{aligned} \tag{B.1}$$

Pore-air mass balance equation:

$$\begin{aligned}
&\phi(1-S)\frac{\partial\rho_a}{\partial t} - \phi\rho_a\frac{\partial S}{\partial t} + (1-S)\rho_a\left[\frac{(1-\phi)}{\rho_s}\frac{\partial\rho_s}{\partial t} + \frac{\partial\varepsilon_v}{\partial t}\right] \\
&- \nabla\cdot\phi(1-S)\rho_a k\frac{k_{ra}}{\mu_a}\nabla(P_a - \rho_a g) = [(1-S)\phi S\rho_a/\rho_s] \\
&\times\{2m_{hc0}(0.187x_{C_3S} + 0.158x_{C_2S} + 0.665x_{C_3A} \\
&+ 0.2130x_{C_4AF})\left\{\left(\frac{\tau}{t_e}\right)^{\beta}\left(\frac{\beta}{t_e}\right)\xi\exp\left[\frac{E_a}{R}\left(\frac{1}{273+T_r} - \frac{1}{273+T}\right)\right]\right\}\}
\end{aligned} \tag{B.2}$$

Momentum balance equation:

$$\nabla\cdot\left(\frac{\partial\sigma}{\partial t}\right) + \frac{\partial[(1-\phi)\rho_s + \phi S\rho_w + \phi(1-S)\rho_a]}{\partial t}g = 0 \tag{B.3}$$

Energy balance equation:

$$\begin{aligned}
&\left[\left(\frac{1}{1+e}\right)\rho_s C_s + \frac{e}{1+e}S\rho_w C_w + \frac{e}{1+e}(1-S)\rho_a C_a\right]\frac{\partial T}{\partial t} \\
&+ \nabla\cdot\left(-k_{eff}\nabla T\right) + \left(\rho_w C_w v^{rw} + \rho_a C_a v^{ra}\right)\cdot\nabla T \\
&= \left(H_c\cdot X_c + 461\cdot X_{slag} + 1800\cdot x_{CaO/FA}\cdot X_{FA}\right)C_b\left(\frac{\tau}{t_e}\right)^{\beta} \\
&\cdot\left(\frac{\beta}{t_e}\right)\cdot\xi\cdot\exp\left[\frac{E_a}{R}\left(\frac{1}{273+T_r} - \frac{1}{273+T}\right)\right]
\end{aligned} \tag{B.4}$$

where ϕ denotes CPB porosity; ρ_i refers to the density (i = air, water and solid); ε_v represents the volumetric strain; k is the intrinsic permeability of CPB; k_{rw} and k_{ra} respectively stands for the relative permeability of pore water and pore air; μ_w and μ_a refer to the dynamic viscosity of pore water and pore air; $\boldsymbol{g}$ is the acceleration of gravity; m_{hc0} denotes the initial cement mass; C_i refers to the specific heat capacity (i = air, water and solid); k_{eff} represents the effective thermal conductivity; $\mathbf{v}^{rw}$ and $\mathbf{v}^{ra}$ respectively refer to Darcy's velocity of pore water and pore air; H_c is the total heat released by hydration; C_b stands for the apparent binder density relative to the total volume of the CPB mixture. The detailed information on the development of constitutive relations and determination of prediction functions of material properties for the fully coupled THMC model are provided in (Cui and Fall 2015a).

Appendix C. Multiphysics Consolidation Model

The multiphysics consolidation model (Cui and Fall 2016c) was derived from the principle of pore space continuity (i.e., volume change of solid phase and skeleton must equal the volume change of pore water and pore air):

$$\begin{aligned}
&\left\{[SP_w + (1-S)P_a]\frac{1-2\upsilon_b}{E_b}\frac{\partial\alpha_{Biot}}{\partial\xi}\right. \\
&-\frac{[\sigma + \alpha_{Biot}[SP_w + (1-S)P_a]]}{E_b}\left\{\frac{9[1-2\upsilon_b]}{E_b}\frac{\partial E_b}{\partial\xi} + 18\frac{\partial\upsilon_b}{\partial\xi}\right\} \\
&-\alpha_{Biot}(P_a - P_w)\frac{1-2\upsilon_b}{E_b}\left\{[1 - S_e(P_w, P_a, \xi)]\frac{\partial\theta_r}{\partial\xi} + \left(\frac{e}{1+e} - \theta_r\right)\frac{\partial S_e}{\partial\xi}\right\} \\
&\left.-\frac{(1+e)(v_n + v_{ab-w})R_{n-w/hc}}{(w/c)v_w + v_c + (1/C_m - 1)v_{tailings}}\right\}\frac{\partial\xi}{\partial t} + \frac{1-2\upsilon_b}{E_b}\frac{\partial\sigma}{\partial t} \\
&+\alpha_{Biot}\frac{1-2\upsilon_b}{E_b}\left\{S - (P_a - P_w)\left(\frac{e}{1+e} - \theta_r\right)\frac{\partial S_e}{\partial P_w}\right\}\frac{\partial P_w}{\partial t} \\
&+\frac{\partial\lambda}{\partial t}\frac{\partial Q_{CTB}}{\partial I_1} + \alpha_{Ts}\frac{\partial T}{\partial t} + \alpha_{Biot}\frac{1-2\upsilon_b}{E_b} \\
&\left\{(1-S) - (P_a - P_w)\left(\frac{e}{1+e} - \theta_r\right)\frac{\partial S_e}{\partial P_a}\right\}\frac{\partial P_a}{\partial t} \\
&= -\left\{\frac{1}{1+e} + \alpha_{Biot}(P_a - P_w)\frac{1-2\upsilon_b}{e^2(1+e)E_b}\left[S_e e + (1+e)^2(1-S_e)\theta_r\right]\right\}\frac{\partial e}{\partial t}
\end{aligned} \tag{C.1}$$

where S_e refers to the effective degree of saturation (i.e., $S_e = (\theta - \theta_r)/(\theta - \theta_r)(\theta_s - \theta_r).(\theta_s - \theta_r)$, θ, θ_s and θ_r are the volumetric, saturated and residual water contents, respectively); λ is a non-negative plastic multiplier; Q_{CTB} is a plastic potential function; α_{Ts} is the coefficient of the thermal expansion (CTE) of the CPB solid phase. Detailed information about the consolidation model is provided in (Cui and Fall 2016c).

References

Abdelaal, A. M. G. M. I. (2011). *Early age mechanical behavior and stiffness development of cemented paste backfill with sand*. Cananda: University of Toronto.

Aldhafeeri, Z., & Fall, M. (2016). Time and damage induced changes in the chemical reactivity of cemented paste backfill. *Journal of Environmental Chemical Engineering, 4*(4), 4038–4049.

Aldhafeeri, Z., & Fall, M. (2017). Sulphate induced changes in the reactivity of cemented tailings backfill. *International Journal of Mineral Processing, 16,* 13–23.

Barnett, S., Soutsos, M., Millard, S., & Bungey, J. (2006). Strength development of mortars containing ground granulated blast-furnace slag: Effect of curing temperature and determination of apparent activation energies. *Cement and Concrete Research, 36*(3), 434–440.

Belem, T., Benzaazoua, M., & Bussière, B. (2000). Mechanical behavior of cemented paste backfill. In *Proceedings of 53rd Canadian Geotechnical Conference Montreal* (pp. 373–380).

Belem, T., El Aatar, O., Bussière, B., Benzaazoua, M., Fall, M., & Yilmaz, E. (2006). Characterization of self-weight consolidated paste backfill. In *Proceedings of the 9th Int. Seminar on Paste and Thickened Tailings* (pp. 333–345).

Bittnar, Z. (2006). Microstructure-based micromechanical prediction of elastic properties in hydrating cement paste. *Cement and Concrete Research, 36*(9), 1708–1718.

Boumiz, A., Vernet, C., & Tenoudji, F. C. (1996). Mechanical properties of cement pastes and mortars at early ages: Evolution with time and degree of hydration. *Advanced Cement Based Materials, 3*(3), 94–106.

Brouwers, H. (2004). The work of Powers and Brownyard revisited: Part 1. *Cement and Concrete Research, 34*(9), 1697–1716.

Célestin, J. C. H., & Fall, M. (2009). Thermal conductivity of cemented paste backfill material and factors affecting it. *International Journal of Mining, Reclamation and Environment, 23*(4), 274–290.

Cihangir, F., Ercikdi, B., Kesimal, A., Deveci, H., & Erdemir, F. (2015). Paste backfill of high-sulphide mill tailings using alkali-activated blast furnace slag: Effect of activator nature, concentration and slag properties. *Minerals Engineering, 83,* 117–127.

Cihangir, F., Ercikdi, B., Kesimal, A., Turan, A., & Deveci, H. (2012). Utilisation of alkali-activated blast furnace slag in paste backfill of high-sulphide mill tailings: Effect of binder type and dosage. *Minerals Engineering, 30,* 33–43.

Comsol (2015). Comsol Multiphysics 5.1, http://www.comsol.com.

Cui, L. (2017). *Multiphysics Modeling and Simulation of the Behavior of Cemented Tailings Backfill*. Ottawa, ON: University of Ottawa.

Cui, L., & Fall, M. (2015a). A coupled thermo-hydro-mechano-chemical model for underground cemented tailings backfill. *Tunnelling and Underground Space Technology, 50,* 396–414.

Cui, L., Fall, M. (2015b).

Cui, L., & Fall, M. (2016a). An evolutive elasto-plastic model for cemented paste backfill. *Computers and Geotechnics, 71,* 19–29.

Cui, L., & Fall, M. (2016b). Mechanical and thermal properties of cemented tailings materials at early ages: Influence of initial temperature, curing stress and drainage conditions. *Construction and Building Materials, 125,* 553–563.

Cui, L., & Fall, M. (2016c). Multiphysics model for consolidation behaviour of cemented paste backfill. *International Journal of Geomechanics, 17*(3), 04016077.

Cui, L., & Fall, M. (2017a). Modeling of pressure on retaining structures for underground fill mass. *Tunnelling and Underground Space Technology, 69,* 94–107.

Cui, L., & Fall, M. (2017b). Modeling of self-desiccation in cemented tailings backfill structure. *International Journal For Numerical and Analytical Methods In Geomechanics*. https://doi.org/10.1002/nag.2756.

Cui, L., & Fall, M. (2017c). Multiphysics modeling of arching effects in fill mass. *Computers and Geotechnics, 83,* 114–131.

Donovan, J. G. (1999). *The effects of backfilling on ground control and recovery in thin-seam coal mining*. Blacksburg, VA: Virginia Polytechnic Institute and State University.

Ercikdi, B., Kesimal, A., Cihangir, F., Deveci, H., & Alp, İ. (2009). Cemented paste backfill of sulphide-rich tailings: Importance of binder type and dosage. *Cement & Concrete Composites, 31*(4), 268–274.

Ercikdi, B., Yılmaz, T., & Külekci, G. (2014). Strength and ultrasonic properties of cemented paste backfill. *Ultrasonics, 54*(1), 195–204.

Fall, M., Belem, T., Samb, S., & Benzaazoua, M. (2007). Experimental characterization of the stress-strain behaviour of cemented paste backfill in compression. *Journal of Materials Science, 42*(11), 3914–3922.

Fall, M., & Benzaazoua, M. (2005). Modeling the effect of sulphate on strength development of paste backfill and binder mixture optimization. *Cement and Concrete Research, 35*(2), 301–314.

Fall, M., Benzaazoua, M., & Saa, E. (2008). Mix proportioning of underground cemented tailings backfill. *Tunnelling and Underground Space Technology, 23*(1), 80–90.

Fall, M., Célestin, J., Pokharel, M., & Touré, M. (2010). A contribution to understanding the effects of curing temperature on the mechanical properties of mine cemented tailings backfill. *Engineering Geology, 114*(3), 397–413.

Fall, M., & Nasir, O. (2010). Mechanical behaviour of the interface between cemented tailings backfill and retaining structures under shear loads. *Geotechnical and Geological Engineering, 28*(6), 779–790.

Fall, M., Nasir, O., Cui, L., & Han, F. S. (2015). Coupled modeling of the strength development and distribution within cemented paste backfill Structure. In *49th US Rock Mechanics/Geomechanics Symposium held in San Francisco, CA, USA, 28 June–1 July 2015*. Copyright 2015 ARMA, American Rock Mechanics Association. Paper 587.

Galaa, A. M., Thompson, B. D., Grabinsky, M. W., & Bawden, W. F. (2011). Characterizing stiffness development in hydrating mine backfill using ultrasonic wave measurements. *Canadian Geotechnical Journal, 48*(8), 1174–1187.

Ghirian, A., & Fall, M. (2013). Coupled thermo-hydro-mechanical-chemical behaviour of cemented paste backfill in column experiments. Part I: Physical, hydraulic and thermal processes and characteristics. *Engineering Geology, 164,* 195–207.

Ghirian, A., & Fall, M. (2014). Coupled thermo-hydro-mechanical-chemical behaviour of cemented paste backfill in column experiments: Part II: Mechanical, chemical and microstructural processes and characteristics. *Engineering Geology, 170,* 11–23.

Ghirian, A., & Fall, M. (2015). Coupled behavior of cemented paste backfill at early ages. *Geotechnical and Geological Engineering, 33*(5), 1141–1166.

Ghirian, A., & Fall, M. (2016a). Long-term coupled behaviour of cemented paste backfill in load cell experiments. *Geomechanics and Geoengineering, 11*(4), 237–251.

Ghirian, A., & Fall, M. (2016b). Strength evolution and deformation behaviour of cemented paste backfill at early ages: Effect of curing stress, filling strategy and drainage. *International Journal of Mining Science and Technology, 26*(15), 809–817.

Hamberg, R., Maurice, C., & Alakangas, L. (2015). The use of low binder proportions in cemented paste backfill—effects on As-leaching. *Minerals Engineering, 78,* 74–82.

Janotka, I. (2001). Hydration of the cement paste with Na_2CO_3 addition. *Ceramics-Silikaty, 45*(1), 16–23.

Jefferis, S., & Wilson, S. (2012). Mine paste backfill-the use of grouts at massive scale. *Grouting and Deep Mixing, 2012,* 1879–1888.

Jiang, H., Fall, M., & Cui, L. (2016). Yield stress of cemented paste backfill in sub-zero environments: Experimental results. *Minerals Engineering, 92,* 141–150.

Jiang, H., Fall, M., & Cui, L. (2017). Freezing behaviour of cemented paste backfill material in column experiments. *Construction and Building Materials, 147,* 837–846.

Koupouli, N. J., Belem, T., Rivard, P., & Effenguet, H. (2016). Direct shear tests on cemented paste backfill-rock wall and cemented paste backfill-backfill interfaces. *Journal of Rock Mechanics and Geotechnical Engineering, 8,* 472–479.

Li, L., & Aubertin, M. (2009). Numerical investigation of the stress state in inclined backfilled stopes. *International Journal of Geomechanics, 9*(2), 52–62.

Li, W., & Fall, M. (2016). Sulphate effect on the early age strength and self-desiccation of cemented paste backfill. *Construction and Building Materials, 106,* 296–304.

Luo, X., Were, P., Liu, J., & Hou, Z. (2015). Estimation of Biot's effective stress coefficient from well logs. *Environmental Earth Sciences, 73*(11), 7019–7028.

Lura, P., Jensen, O. M., & van Breugel, K. (2003). Autogenous shrinkage in high-performance cement paste: An evaluation of basic mechanisms. *Cement and Concrete Research, 33*(2), 223–232.

Mozaffaridana, M. (2011). *Using thermal profiles of cemented paste backfill to predict strength*. Toronto, ON: University of Toronto.

Nasir, O., & Fall, M. (2009). Modeling the heat development in hydrating CPB structures. *Computers and Geotechnics, 36*(7), 1207–1218.

Nasir, O., & Fall, M. (2010). Coupling binder hydration, temperature and compressive strength development of underground cemented paste backfill at early ages. *Tunnelling and Underground Space Technology, 25*(1), 9–20.

Qi, C., Fourie, A., & Chen, Q. (2018). Neural network and particle swarm optimization for predicting the unconfined compressive strength of cemented paste backfill. *Construction and Building Materials, 159,* 473–478.

Rankine, R. M., & Sivakugan, N. (2007). Geotechnical properties of cemented paste backfill from Cannington Mine, Australia. *Geotechnical and Geological Engineering, 25*(4), 383–393.

Sargeant, A.L. (2008). The Application of Post Consumer Glass as a Cementing Agent in Mine Backfill (Doctoral dissertation).

Schindler, A. K., & Folliard, K. J. (2003). Influence of supplementary cementing materials on the heat of hydration of concrete. In *Proceedings of advance in cement and concrete IX conference* (pp. 1–10). Colorado.

Smilauer, V., & Bittnar, Z. (2006). Microstructure-based micromechanical prediction of elastic properties in hydrating cement paste. *Cement and Concrete Research, 36*(9), 1708–1718.

Suazo, G., Fourie, A., & Doherty, J. (2016a). Cyclic shear response of cemented paste backfill. *Journal Of Geotechnical and Geoenvironmental Engineering, 143*(1), 04016082.

Suazo, G., Fourie, A., & Doherty, J. (2016b). Experimental study of the evolution of the soil water retention curve for granular material undergoing cement hydration. *Journal Of Geotechnical and Geoenvironmental Engineering, 142*(7), 04016022.

Veenstra, R. L. (2013). *A design procedure for determining the in situ stresses of early age cemented paste backfill*. Toronto, ON: University of Toronto.

Veenstra, R., Bawden, W., Grabinsky, M., & Thompson, B. (2011). An approach to stope scale numerical modelling of early age cemented paste backfill. In *Proceedings 45th US Rock Mechanics/Geomechanics Symposium, American Rock Mechanics Association* (pp. 1–7).

Wang, Y., & Fall, M. (2014). Initial temperature-dependence of strength development and self-desiccation in cemented

paste backfill that contains sodium silicate. *Cement & Concrete Composites, 67,* 101–110.

Wu, D., Fall, M., & Cai, S. (2013). Coupling temperature, cement hydration and rheological behaviour of fresh cemented paste backfill. *Minerals Engineering, 42,* 76–87.

Wu, A., Wang, Y., Zhou, B., & Shen, J. (2016). Effect of initial backfill temperature on the deformation behavior of early age cemented paste backfill that contains sodium silicate. *Advances in Materials Science and Engineering*. https://doi.org/10.1155/2016/8481090.

Xu, S., Suorineni, F. T., Li, K., & Li, Y. (2017a). Evaluation of the strength and ultrasonic properties of foam-cemented paste backfill. *International Journal of Mining, Reclamation and Environment, 31*(8), 544–557.

Xu, W., Tian, X., & Cao, P. (2017b). Assessment of hydration process and mechanical properties of cemented paste backfill by electrical resistivity measurement. *Nondestructive Testing and Evaluation*. https://doi.org/10.1080/10589759.2017.1353983.

Ye, G., Sun, Z., Voigt, T., Van Breugel, K., Shah, S. (2004). A micromechanic model for characterization of cement paste at early age validated with experiments. In Proceedings of the RILEM International Symposium on Advances in Concrete through Science and Engineering.

Yilmaz, E., Belem, T., & Benzaazoua, M. (2015). Specimen size effect on strength behavior of cemented paste backfills subjected to different placement conditions. *Engineering Geology, 185,* 52–62.

Yilmaz, E., Belem, T., Bussière, B., & Benzaazoua, M. (2011). Relationships between microstructural properties and compressive strength of consolidated and unconsolidated cemented paste backfills. *Cement & Concrete Composites, 33*(6), 702–715.

Yılmaz, T., & Ercikdi, B. (2016). Predicting the uniaxial compressive strength of cemented paste backfill from ultrasonic pulse velocity test. *Nondestructive Testing and Evaluation, 31*(3), 247–266.

Yılmaz, T., Ercikdi, B., Karaman, K., & Külekçi, G. (2014). Assessment of strength properties of cemented paste backfill by ultrasonic pulse velocity test. *Ultrasonics, 54*(5), 1386–1394.